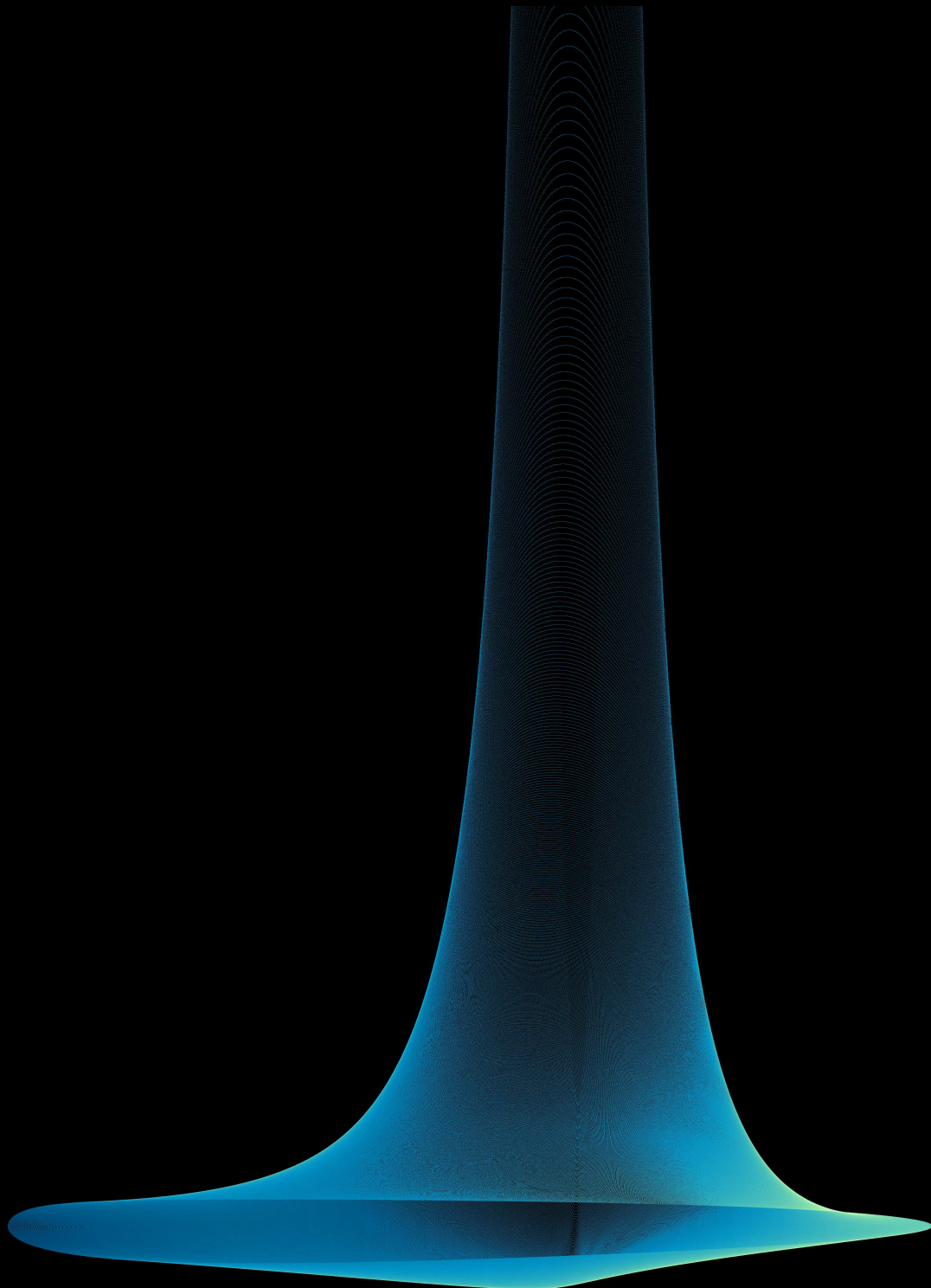


---

# Reverberation Mapping of Flared Accretion Discs

---

Fabian Brod







Dr. Karl Remeis Sternwarte Bamberg  
Astronomisches Institut der Universität Erlangen-Nürnberg

## DIPLOMARBEIT

---

# REVERBERATION MAPPING OF FLARED ACCRETION DISCS

---

**Fabian Brod**

supervised by  
Prof. Dr. Jörn Wilms

Bamberg, 12.09.2013



ERLANGEN CENTRE  
FOR ASTROPARTICLE  
PHYSICS

**Friedrich-Alexander-Universität  
Erlangen-Nürnberg**



Image on the title page: *Transfer function of energy and time for an inclination of  $70^\circ$ . It illustrates the dynamical spectrum of a broad iron line, emitted by a flared accretion disc. See Section 3.11 for more details.*

---

# CONTENTS

---

<b>Deutsche Zusammenfassung</b>	<b>1</b>
<b>Abstract</b>	<b>2</b>
<b>1 Introduction</b>	<b>3</b>
<b>2 Theory</b>	<b>7</b>
2.1 Geometry of the system . . . . .	7
2.2 Photon trajectories and travel times . . . . .	8
2.3 Irradiation of the accretion disc . . . . .	11
2.4 Energy shifts . . . . .	13
2.4.1 Gravitational energy shift . . . . .	13
2.4.2 Doppler shift and aberration . . . . .	14
2.5 Observed Flux . . . . .	15
2.5.1 Visibility . . . . .	15
<b>3 Simulation and results</b>	<b>17</b>
3.1 Irradiation of the accretion disc . . . . .	17
3.1.1 Flux of an anisotropic source . . . . .	20
3.2 Radiation transport from disc to observer . . . . .	20
3.3 Calculating time lags and emission line spectra . . . . .	22
3.4 The observed flux . . . . .	23
3.5 Test of the simulation . . . . .	26
3.6 Time delay in flat and curved spacetime . . . . .	26
3.7 Covering effects . . . . .	27
3.8 Parameter dependency of time delays and broad iron lines . . . . .	29
3.8.1 Inclination . . . . .	29
3.8.2 Height of the accretion disc . . . . .	30
3.8.3 Curvature of the accretion disc . . . . .	33
3.8.4 Height of the primary source . . . . .	34
3.9 Geometric origin of the peaks in time lags . . . . .	35
3.10 Time lags for anisotropic sources . . . . .	37
3.11 Transfer functions . . . . .	37
<b>4 Conclusion and outlook</b>	<b>44</b>
<b>Acknowledgments</b>	<b>46</b>
<b>References</b>	<b>47</b>
<b>Declaration</b>	<b>48</b>

---

# DEUTSCHE ZUSAMMENFASSUNG

---

Inhalt dieser Diplomarbeit ist eine allgemein-relativistische Betrachtung des Prinzips des “reverberation mapping” von Akkretionsscheiben, wie sie in Doppelsternsystemen, bestehend aus einem schwarzen Loch und einem Stern, und aktiven galaktischen Kernen beobachtet werden. Eine Simulation zur Berechnung des Zeitversatzes (“time lag”) von gemessener primärer und reflektierter Strahlung solcher Systeme, die durch die “lamp post” Geometrie beschrieben werden wurde entwickelt. Dabei werden unter anderem die Bestrahlung der Akkretionsscheibe, die beobachteten Spektren von Emissionslinien sowie angesprochene time lags berechnet. Die zugrunde liegende Theorie wird präsentiert und teilweise hergeleitet.

Die Bestrahlung der Akkretionsscheibe durch isotrope und nicht isotrope Quellen wird ebenso behandelt wie die geometrische Verteilung von Energieverschiebung, time delay und dem vom Beobachter gemessenen Fluss.

Als Test für die Simulation werden Spektren von Emissionslinien flacher Akkretionsscheiben mit analogen Ergebnissen der bereits etablierten *relline* Simulation verglichen. Das Ergebnis ist eine gute Übereinstimmung beider Modelle.

Es wird nachgewiesen, dass sich die time lags für gekrümmte Raumzeit auf der einen und flache Raumzeit auf der anderen Seite signifikant voneinander unterscheiden, was belegt dass eine allgemein-relativistische Herangehensweise bei der Behandlung dieses Themas notwendig ist. Das System aus schwarzem Loch, Akkretionsscheibe und primärer Strahlungsquelle ist charakterisiert durch die Höhe der Quelle über dem schwarzen Loch, der Höhe der der Akkretionsscheibe und deren Krümmung sowie der Inklination des Beobachters. Die Abhängigkeit der time lags und der gemessenen Spektren der Emissionslinien von diesen Parametern wird detailliert behandelt. Weiterhin wird genauer auf die Unterschiede in der Parameterabhängigkeit von klassischem und relativistischem time delay eingegangen.

Ferner werden Transferfunktionen für Energie und Zeit gezeigt. Diese illustrieren anschaulich die zeitliche Dynamik der gemessenen Emissionslinien. Den Abschluss der Arbeit bildet die Motivation möglicher Erweiterungen des Modells.

---

# ABSTRACT

---

Content of this diploma thesis is a general relativistic approach to reverberation mapping of flared accretion discs, as they can be found in binary black holes or active galactic nuclei (AGN). A numerical simulation for the calculation of time lags for black hole systems, described by the lamp post geometry, is developed. Among others, it computes the irradiation of the accretion disc, the observed spectra for fluorescent emission lines and the time delays. The underlying theory is presented and partly derived.

The illumination of the accretion disc by isotropic and anisotropic primary sources is presented, as well as the distribution of energy shift, time delay and observed flux.

To test the simulation, emission line spectra are compared with results obtained from the approved relline simulation for the case of a flat accretion disc. The yielded accordance is satisfying.

It is shown that the time lags calculated for a curved spacetime significantly differ from those obtained in the Euclidean case of flat space. This means that a general relativistic treatment of the subject is necessary. The parameters describing the black hole system are the height of the irradiating source, the height and curvature of the accretion disc and the inclination of the distant observer. The dependency of time lags and emission line spectra on them is investigated in detail. Further, the different behavior of the time lags and their non-relativistic equivalents under changes of these parameters is discussed.

Moreover, transfer functions for time delay and energy shift, which illustrate the dynamical spectrum of the broad emission lines, are presented. At last, possible extensions of the simulation are motivated.

---

# CHAPTER 1

## INTRODUCTION

---

The presentation of the theory of general relativity by Albert Einstein (1916) was a paradigm shift for physics and a whole new branch of science was created on this basis. Soon after his discovery, the first solution of his field equations describing the effects of matter on spacetime was found by Karl Schwarzschild (1916). He developed his metric in order to describe the external field of a static star. But there is more to it: imagine there is no star to create the field. One might think the Schwarzschild spacetime would then be that of a point like mass located at the origin of coordinates – which turns out to be wrong. It rather represents a wormhole, created by two joining singularities in two asymptotically flat universes, connecting them at first, then expanding and finally recontracting until split off, each universe remaining with its own singularity (Misner et al., 1973).

This *is* an exact solution to the Einstein field equations. But are there such wormholes out there in the universe? The answer is: probably not. First of all the evolution described above could only happen if the universe was born with certain initial conditions, which is somewhat unlikely. Second, we simply don't see any evidence of them.

So, why is the Schwarzschild solution so relevant? Because, truncated appropriately, it describes the spacetime around black holes, for which we *do* have evidence.

There are essentially two types of black holes in the universe, such with stellar mass and others with up to billions times the mass of our sun ( $M_{\odot}$ ). The first type is the last stage of the life of stars at least 10 to 15 times as massive as the sun (typically more than  $50M_{\odot}$ ). At the end of their lifetime they explode in a supernova, and as there is nothing to compensate the gravitational forces that act on the remnant, it undergoes a gravitational collapse, forming a black hole of about some tens of kilometers in diameter (Krolik, 1999; Longair, 2011). Such an isolated black hole would be hard to detect, as all it emits is Hawking radiation while slowly evaporating (Hawking, 1974). On the other hand, a huge amount of X-ray radiation is produced when interacting with matter. This matter could either be interstellar clouds or material of a companion star (binary black holes), while the second case is the more relevant. Either way, as the matter falls into the black hole it forms an accretion disc and its kinetic energy increases. In addition tidal forces act on it which leads to a heating up to several million degrees. This causes the atoms to emit X-ray radiation with a very high energy release efficiency (Rees et al., 1982; Shakura & Sunyaev, 1973; Frank et al., 1995) before falling into the singularity.

The second type, the supermassive black holes, were formed in the center regions of young galaxies when stars collided and merged into a giant black hole (Krolik, 1999). Accreting more and more mass from passing by stars or interstellar medium, the black holes can reach a mass of up to about  $10^9 M_{\odot}$ . Just as in the case of stellar mass black holes, the matter forms an accretion disc while falling into the black hole, emitting light in the whole electromagnetic

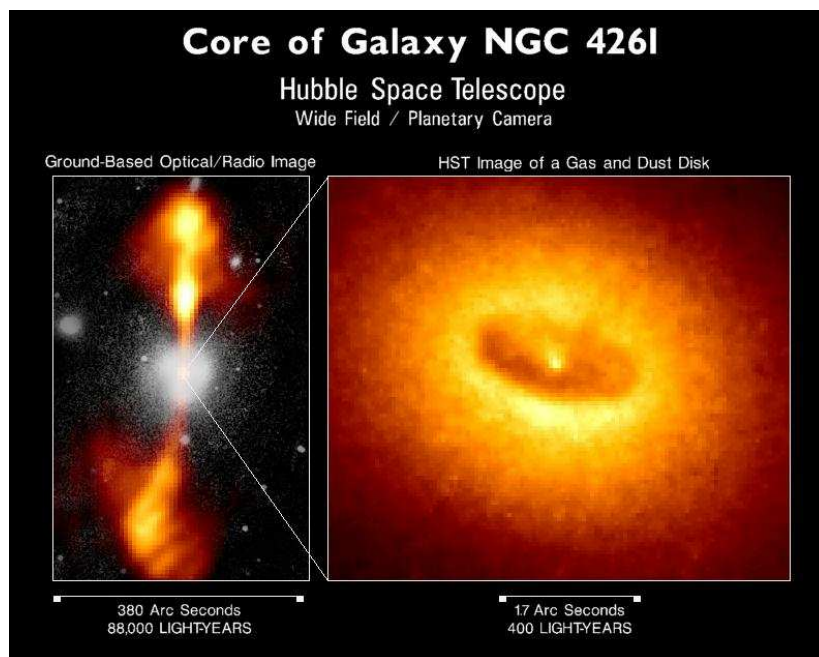


Fig. 1.1: Core of the galaxy NGC4261 in the virgo cluster. Picture from (Ferrarese et al., 1996).

spectrum. Since these objects are found in the center of galaxies they are also referred to as “active galactic nuclei” (AGN).

AGN can again be divided into two classes. A fraction of them form highly collimated beams (‘jets’) of high-energetic particles which are accelerated perpendicular to the accretion disc to almost the speed of light (Marscher, 2006). The physics responsible for this process is not yet understood very well. Nevertheless, these jets emit huge amounts of radiation in the radio wavelengths. Sources whose overall luminosity is dominated by this radiation are called radio-loud. There are more subclasses of radio-loud objects, such as quasars, blazars and radio galaxies, depending on their spectra, luminosity and observed emission lines. Sources without jets or jets that do not contribute significantly to the luminosity are the so called radio-quiet AGN, among others the Seyfert galaxies (Antonucci, 1993). Figure 1.1 shows a optical and radio image of the active galaxy NGC 4261.

The problem with examining AGN or binary black holes is that the the angular resolution of satellites or telescopes is not sufficient to spatially resolve their inner structure (Netzer & Peterson, 1997). Fortunately, there is another way to probe them, so called reverberation mapping, firstly presented by Blandford & McKee (1982): the rate at which mass is accreted by the black hole is not steady. As this rate undergoes variations, so does the flux that can be observed. The X-ray spectrum consists of a cut-off power-law shaped continuum (combining the effects of thermal Comptonization on the inner accretion flow (Sunyaev & Titarchuk, 1980), magnetic flares over the inner disc (Beloborodov, 1999), contributions of base of the jet (Markoff et al., 2001) and more), soft black-body emission from the accretion disc and a Compton continuum with emission lines broadened by Doppler shifts (e.g. and most important the  $K_{\alpha}$  iron line at 6.4keV) reflected from the disc (George & Fabian, 1991; Nandra & Pounds, 1994).

The radiation reflected from the accretion disc is delayed with respect to the primary radiation. Figure 1.2 shows the light curve of the Seyfert 1 galaxy 3C120. The B band represents the primary radiation, the  $H_{\beta}$  light curve the response of the accretion disc. For more details

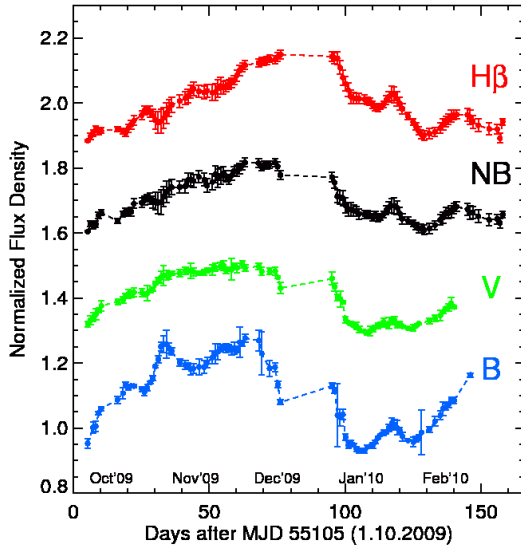


Fig. 1.2: Light curves for different optical bands for the Seyfert 1 galaxy 3C120 showing the time lag between primary and reflected radiation. See text for more details. Picture taken from Pozo Nuñez et al. (2012).

on the different energy bands see Pozo Nuñez et al. (2012). The steep decrease in flux in the B band in the beginning of December 2009 is followed by the same pattern in the reflected light curve in the end of December. So a rough estimation of the time delay between primary and reflected spectrum is about 25 days. Determining the time lag in detail requires cross-correlating the two light curves. The result can be seen in figure 1.3. The idea of reverberation mapping is to analyze the magnitude and exact shape of such cross correlations (time lags) in order to obtain information about the black hole system, like mass, spin or the geometry of source and accretion disc.

The standard model for accretion discs by Shakura & Sunyaev (1973) describes a geometrical thin and optical thick disc with height  $H \propto r/H$ . Observations suggest that the accretion discs of many X-ray binaries are likely to be flared (Poutanen, 2002). This issue has been treated (Poutanen, 2002; Cassatella et al., 2011, 2012), but so far there is no general relativistic

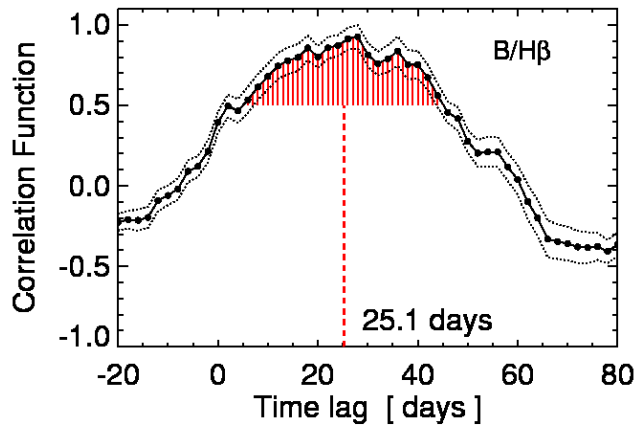


Fig. 1.3: Cross correlation of the  $H\beta$  and B band light curves. The dotted lines indicate the error range ( $\pm 1\sigma$ ). Picture taken from Pozo Nuñez et al. (2012).

tic model considering the effects of light bending near compact objects for time delays of such flared accretion discs. So the aim of this thesis is to develop a model to compute these relativistic time lags, compare them with the case of a flat spacetime, and investigate how changes in the system parameters affect them.

The remainder of this thesis is structured as follows. In Chapter 2 the underlying theory is presented. Chapter 3 contains the results of the developed model and their interpretation, particularly the comparison of time lags in flat a curved spacetime. Finally a conclusion and a prospect to possible further developments are given in Chapter 4.

---

## CHAPTER 2

# THEORY

---

In this chapter the geometry of the problem and the necessary theory are presented. Basis is the Schwarzschild solution of the Einstein field equations, which describes a non-rotating black hole. For the sake of generality at some points the Kerr-metric is used, considering a non-zero spin of the black hole. Nevertheless, all formulas transition into the corresponding Schwarzschild formulas for zero spin. After defining the basic setup, photon trajectories and travel times are derived starting from the metric. The essential formulas for the irradiation of the accretion disc, the energy shift and the observed flux are given and partly derived. Throughout this thesis the speed of light and the gravitational constant are set to unity,  $G \equiv c \equiv 1$ . Unless stated otherwise, this presentation follows Misner et al. (1973).

### 2.1 GEOMETRY OF THE SYSTEM

The underlying geometry of the problem is quite simple. The black hole is at the origin. The accretion disc is considered to be axially symmetric, with the  $z$ -axis being the symmetry axis. The height above the equatorial plane is given by a power-law (compare Poutanen, 2002):

$$z(r) = H \left( \frac{r}{r_{\text{out}}} \right)^\zeta, \quad (2.1)$$

with the maximum height of the disc  $H$  and the disc's radius  $r_{\text{out}}$ . The minimal radius  $r_{\text{min}}$  of the disc is discussed later on. The primary radiation source is situated on the symmetry axis at height  $h$  ( $\mathbf{h} = (0, 0, h)$ ) and its angular distribution is assumed not to depend on time or energy of the emitted photons. The direction under which the distant observer is looking at the system is defined by the inclination vector

$$\mathbf{i} = \begin{pmatrix} \sin i \\ 0 \\ \cos i \end{pmatrix} \quad (2.2)$$

with inclination angle  $i$ . This geometry is also called the 'lamp post geometry' (see, e.g., Dovčiak et al., 2012; Dauser et al., 2013).

## 2.2 PHOTON TRAJECTORIES AND TRAVEL TIMES

The Schwarzschild geometry is described by the line element

$$ds^2 = -\left(1 - \frac{r_s}{r}\right) dt^2 + \frac{dr^2}{\left(1 - \frac{r_s}{r}\right)} + r^2 (d\theta^2 + \sin^2\theta d\phi^2) \quad (2.3)$$

in spherical coordinates  $x^\mu = (t, r, \theta, \phi)$ , where  $r_s = 2M$  is the Schwarzschild radius. In terms of the metric  $g_{\mu\nu}$  the line element is

$$ds^2 = g_{\mu\nu} dx^\mu dx^\nu. \quad (2.4)$$

This expression holds outside any spherical symmetric center of attraction with mass  $M$  (e.g., a star), and in particular a system that has undergone complete gravitational collapse, i.e. a black hole. In the latter case Eq. (2.3) applies arbitrarily close to  $r_s$ , where the line element has a singularity. Note that this singularity is not an essential one but rather due to the choice of coordinates, but since we are only interested in the region outside the Schwarzschild radius the chosen coordinate system is sufficient.

Projecting the location of a test particle onto the unit sphere, this projected point defines, together with the particle's 3-velocity, a great circle on the sphere. As the particle keeps moving, the radial projection of its position remains on this very great circle, as choosing the one or the other hemisphere would mean to break the symmetry of the situation. It is convenient to orient the system so that the orbit lies in the equatorial plane ( $\theta = \pi/2$ ), and since the particle wont leave it, its momentum in  $\theta$ -direction vanishes:

$$p^\theta = \frac{d\theta}{d\lambda} = 0, \quad (2.5)$$

with the affine parameter  $\lambda$  defined as the fraction of proper time,  $\tau$ , and rest mass,  $\mu$ :

$$\lambda = \frac{\tau}{\mu}. \quad (2.6)$$

Looking at the the line element (2.3) shows that the geometry is invariant under translation of time ( $t \rightarrow t + \Delta t$ ) and  $\phi$  ( $\phi \rightarrow \phi + \Delta\phi$ ), thus the conjugate momenta of these two coordinates are conserved, i.e.,

$$p_0 \equiv -E, \quad p_\phi \equiv \pm L. \quad (2.7)$$

The quantities  $E$  and  $L$  are the particles energy and angular momentum, respectively. Furthermore the invariance under time translations implies the existence of the Killing vector

$$\xi^\mu = (1, 0, 0, 0), \quad (2.8)$$

which will help us to calculate the gravitational redshift later on. The magnitude of the energy-momentum 4-vector is given by

$$g_{\alpha\beta} p^\alpha p^\beta + \mu^2 = g^{\alpha\beta} p_\alpha p_\beta + \mu^2 = 0, \quad (2.9)$$

or, substituting the previous results:

$$-\frac{E^2}{\left(1 - \frac{r_s}{r}\right)} + \frac{1}{\left(1 - \frac{r_s}{r}\right)} \left(\frac{dr}{d\lambda}\right)^2 + \frac{L^2}{r^2} + \mu^2 = 0. \quad (2.10)$$

The equivalence principle of general relativity states that every test particle follows the same trajectory, regardless of its mass. Therefore it is convenient to describe the particles motion in terms of the energy per unit rest mass and angular momentum per unit rest mass,

$$\tilde{E} = \frac{E}{\mu} \quad \text{and} \quad \tilde{L} = \frac{L}{\mu}. \quad (2.11)$$

Equation (2.10) then reads:

$$\left(\frac{dr}{d\tau}\right)^2 = \tilde{E}^2 - \left(1 - \frac{r_s}{r}\right) \left(1 + \frac{\tilde{L}^2}{r^2}\right), \quad (2.12)$$

the change of  $r$  with proper time, independent of the rest mass. The rate of change of the other two relevant coordinates with proper time is given by

$$\frac{d\phi}{d\tau} = \frac{1}{\mu} \frac{d\phi}{d\lambda} = \frac{p^\phi}{\mu} = \frac{g^{\phi\phi} p_\phi}{\mu} = \frac{g^{\phi\phi} L}{\mu} = \frac{\tilde{L}}{r^2}, \quad (2.13)$$

where the orbit with increasing  $\phi$  was chosen (i.e.  $p_\phi = +L$ ), and analogue

$$\frac{dt}{d\tau} = \frac{\tilde{E}}{1 - \frac{r_s}{r}}. \quad (2.14)$$

Substituting  $d\tau$  from Eq. (2.13) into Eq. (2.12) leads to

$$\left(\frac{\tilde{L} dr}{r^2 d\phi}\right)^2 + \left(1 - \frac{r_s}{r}\right) \left(1 + \frac{\tilde{L}^2}{r^2}\right) = \tilde{E}^2. \quad (2.15)$$

In order to obtain the equations of motion for photons (zero rest mass) the limit  $\mu \rightarrow 0$  is to perform. Of course the quantities  $\tilde{E}$  and  $\tilde{L}$  make no sense there, as they go to infinity. However, the ratio

$$b \equiv \frac{L}{\sqrt{E^2 - \mu^2}} = \frac{\tilde{L}}{\sqrt{\tilde{E}^2 - 1}} \quad (2.16)$$

has the finite limit

$$\lim_{\mu \rightarrow 0} \frac{\tilde{L}}{\tilde{E}} = b. \quad (2.17)$$

In this zero-mass limit Eq. (2.15) transforms into

$$\left(\frac{1}{r^2} \frac{dr}{d\phi}\right)^2 + \frac{1 - \frac{r_s}{r}}{r^2} = \frac{1}{b^2}. \quad (2.18)$$

Integrating this equation finally gives an expression of the photon's orbit:

$$\phi(r) = \int \frac{dr}{r^2} \left[ \frac{1}{b^2} - \frac{1}{r^2} \left(1 - \frac{r_s}{r}\right) \right]^{-1/2}. \quad (2.19)$$

One thing worth to point out is that for impact parameters bigger than a critical value,

$$b_c = \frac{3\sqrt{3}}{2} r_s, \quad (2.20)$$

the photons may run through a turning point (also referred to as 'periastron') at (Falkner et al., 2013)

$$r = r_{\text{turn}} \equiv -2\sqrt{\frac{b^2}{3}} \cos\left(\frac{\arccos\left(\frac{3\sqrt{3}}{2} \frac{r_s}{b}\right) + 2\pi}{3}\right), \quad (2.21)$$

thus in this case one has to integrate to this point and then from it to the final  $r$ -value in order to obtain the correct angle  $\phi$ . Rephrasing the conservation laws (2.13) and (2.14) in terms of the affine parameter instead of the proper time gives:

$$\frac{d\phi}{d\lambda} = \frac{L}{r^2}. \quad (2.22)$$

and

$$\frac{dt}{d\lambda} = \frac{E}{1 - \frac{r_s}{r}}. \quad (2.23)$$

Keeping in mind that the photon's path does not depend on the energy or the angular momentum individually, but rather their ratio (i.e., the impact parameter  $b$ ), one can do a transition of the affine parameter

$$\lambda \rightarrow L\lambda. \quad (2.24)$$

Thus Eq. (2.22) transforms into

$$\frac{d\phi}{d\lambda} = \frac{1}{r^2}, \quad (2.25)$$

Eq. (2.23) into

$$\frac{dt}{d\lambda} = \frac{1}{b \left(1 - \frac{r_s}{r}\right)} \quad (2.26)$$

and finally Eq. (2.18) into

$$\frac{dr}{d\lambda} + \frac{1 - \frac{r_s}{r}}{r^2} = \frac{1}{b^2}. \quad (2.27)$$

Equipped with these expressions it is on the one hand possible to give an expression of the photon's travel time,

$$t = \int dt = \int \frac{dt}{d\lambda} \frac{d\lambda}{dr} dr, \quad (2.28)$$

which becomes, using Equations (2.23) and (2.27)

$$t(r) = \int \frac{dr}{1 - \frac{r_s}{r}} \left[ 1 - \frac{b^2}{r^2} \left( 1 - \frac{r_s}{r} \right) \right]^{-1/2}. \quad (2.29)$$

Here, just as in the case of the calculation of  $\phi$ , one has to consider if the turning point lies in the integration interval.

On the other hand looking at the  $\phi$ -component of the unit velocity vector,

$$\hat{v}_\phi = \frac{|g_{\phi\phi}|^{1/2} d\phi/d\lambda}{|g_{00}|^{1/2} dt/d\lambda} = \frac{br}{\sqrt{1 - \frac{r_s}{r}}}, \quad (2.30)$$

it is now possible to express the impact parameter  $b$  in terms of the radius  $R$  at which a photon is emitted and the angle between initial propagation direction and radial direction  $\alpha$ :

$$b = \frac{R \sin \alpha}{\sqrt{1 - \frac{r_s}{R}}}. \quad (2.31)$$

## 2.3 IRRADIATION OF THE ACCRETION DISC

The photon trajectories and travel times in the last section were calculated in Schwarzschild spacetime. Most of the formulae required for the irradiation of the accretion disc presented now will be for the Kerr metric. This is not mandatory, since all the simulations presented in this thesis assume a non-rotating black hole. Nevertheless, in order to provide the basis for an extension to a simulation considering rotating black holes, the more general approach is chosen here. The transition to the corresponding Schwarzschild expressions is performed by setting the spin of the black hole to zero, which can be done at any point.

The line element in the Kerr metric (Kerr, 1963) is given by:

$$ds^2 = -\left(1 - \frac{2Mr}{\Sigma}\right) dt^2 - \frac{4aMr \sin^2 \theta}{\Sigma} dt d\phi + \frac{\Sigma}{\Delta} dr^2 + \Sigma d\theta^2 + \left(r^2 + a^2 + \frac{2a^2 Mr \sin^2 \theta}{\Sigma}\right) \sin^2 \theta d\phi^2. \quad (2.32)$$

Besides the mass  $M$  of the black hole it also considers its spin  $a$ ;  $\Delta = r^2 - 2Mr + a^2$  and  $\Sigma = r^2 + a^2 \cos^2 \theta$ . For zero spin the line element transforms exactly into the line element for the Schwarzschild spacetime (2.3).

The accretion disc consists of gas particles revolving around the black hole. But not all circular orbits are stable, actually there is a certain radius  $r_{min}$  below which all orbits are unstable, that defines the inner edge of the accretion disc. It is given by (Bardeen et al., 1972)

$$r_{min} = M \left(3 + Z_2 \mp [(3 - Z_1)(3 + Z_1 + 2Z_2)]^{1/2}\right), \quad (2.33)$$

where

$$Z_1 \equiv 1 + \left(1 - \frac{a^2}{M^2}\right)^{1/3} \left[\left(1 + \frac{a}{M}\right)^{1/3} + \left(1 - \frac{a}{M}\right)^{1/3}\right], \quad (2.34)$$

$$Z_2 \equiv \left(\frac{3a^2}{M^2} + Z_1^2\right)^{1/2}.$$

In order to calculate the intensity with which the accretion disc is illuminated, the intersection of the photon trajectories (2.19) and the accretion disc (2.1) has to be calculated. If this is done for equally spaced angles  $\alpha$  (the angle between the symmetry axis of the system and the initial direction of the photon emitted at the source), the distance of these intersection points,  $\Delta r$ , is a measure for the incident intensity (see e.g., Wilkins & Fabian, 2012; Dauser et al., 2013). Photons emitted in  $[\alpha; \alpha + \Delta\alpha]$  hit the disc within the interval of radii  $[r; r + \Delta r]$  and are thus distributed on a ring with width  $\Delta r$ . In flat space the area  $A$  of this ring would be  $A(r, \Delta r) = 2\pi \sin \theta r \Delta r$ . The curvature of spacetime near the black hole changes the proper area of the ring.  $\Delta r$  can be split into a parts parallel and perpendicular to the position 3-vector  $\mathbf{r}$  of the intersection:

$$\begin{aligned} d_{\parallel} &= \Delta r \cos \beta, \\ d_{\perp} &= \Delta r \sin \beta, \end{aligned} \quad (2.35)$$

where  $\beta$  is the angle between the surface element  $\Delta r$  and  $\mathbf{h}$ , which can be easily obtained using the derivative of equation (2.1). Since the metric (i.e., the Schwarzschild metric in this case<sup>1</sup>) is invariant under rotation, only the parallel part is affected:

$$\widetilde{d}_{\parallel} = \sqrt{g_{rr}} d_{\parallel}. \quad (2.36)$$

<sup>1</sup>An approach with the Kerr spacetime is possible as well, but somewhat more subtle, since in this case there is no spherical symmetry of the metric.

Using this,  $\Delta r$  becomes

$$\widetilde{\Delta r} = \sqrt{\widetilde{d}_{\parallel}^2 + d_{\perp}^2} = \sqrt{(g_{rr} \cos^2 \beta + \sin^2 \beta) \Delta r^2} \quad (2.37)$$

and thus the rings area is given by

$$A(r, \Delta r, \theta) = 2\pi r \sin \theta \Delta r \sqrt{\frac{1}{1 - \frac{r_s}{r}} \cos^2 \beta + \sin^2 \beta}. \quad (2.38)$$

As the disc rotates at relativistic speed it is contracted in the rest frame of the observer. Since the irradiation in the disc's rest frame is of interest, the area is effectively enlarged with an inverse Lorentz factor. The disc's velocity profile can be calculated as (Bardeen et al., 1972)

$$v^{(\phi)} = \frac{\pm \sqrt{M} (r^2 \mp 2a\sqrt{Mr} + a^2)}{\sqrt{\Delta} (r^{3/2} \pm a\sqrt{M})}. \quad (2.39)$$

Here and in the following the upper sign corresponds to an accretion disc rotating in the same direction as the black hole, the lower sign to the reverse case. This relation was derived for a flat disc in the equatorial plane. For the flared disc it is assumed to be the same, the gas rings are simply 'lifted up'. Nevertheless, this is exact for zero spin, as the circular orbits depend only of the radius.

The corresponding Lorentz factor  $\gamma = (1 - v^2)^{-1/2}$  is (Bardeen et al., 1972)

$$\gamma^{(\phi)} = \frac{\sqrt{\Delta} (r^{3/2} \pm M^{3/2}) (\sqrt{r} \pm \sqrt{M})}{r^{1/4} \sqrt{\sqrt{r} \pm 2\sqrt{M}} \sqrt{r^3 + M^2 r + 2M^3}}. \quad (2.40)$$

These are the geometrical effects contributing to the flux on the disc surface. Together they read:

$$F_i^{\text{geo}} = \frac{\sin \alpha}{A(r, \Delta r, \theta) \gamma^{(\phi)}}. \quad (2.41)$$

The sine in the nominator reflects the assumption of a source that is not point like but rather a sphere, so for angles corresponding to the poles of the source the emission is weaker than for the equator. This term can be substituted by any other distribution. One possible example is radiating plasma, that moves towards or away from the black hole (as for AGN jets), with bulk velocity  $v_{\text{bulk}}$ . Its angular distribution is then given by

$$\Omega(\alpha) = \frac{1}{\gamma_{\text{bulk}}^4 (1 - v_{\text{bulk}} \cos \alpha)^3}, \quad \gamma_{\text{bulk}} = \frac{1}{\sqrt{1 - v_{\text{bulk}}^2}}, \quad (2.42)$$

if the emission is isotropic in the plasma rest frame (Rybicki & Lightman, 1980).

In addition, the relativistic energy shift of the photons, emitted by the source and intercepted by the relatively spinning accretion disc, also affects the incident flux and is given by (Fukumura & Kazanas, 2007; Dauser et al., 2013)

$$g_{lp} = \frac{E_i}{E_e} = \frac{p_{\mu} u_{\text{disc}}^{\mu}}{p_{\nu} u_{\text{source}}^{\nu}} = \frac{(r^{3/2} + a\sqrt{M}) \sqrt{h^2 - 2Mh + a^2}}{\sqrt{r} \sqrt{r^2 - 3Mr + 2a\sqrt{Mr}} \sqrt{h^2 + a^2}} \quad (2.43)$$

Note that this is just an approximation<sup>2</sup> for the same reasons as discussed for the velocity profile of the flared disc and exact only for a flat disc.

The number of photons is conserved, this can be expressed in the relation (see Dauser et al., 2013)

$$N_e \Delta t_e \Delta E_e = \text{const.} = N_i \Delta t_i \Delta E_i, \quad (2.44)$$

where  $N_e$  is the flux of emitted photons and  $N_i$  the of the incident photon, respectively. The emitted radiation is assumed to be described by a power law with photon index  $\Gamma$ ,

$$N_e \sim E_e^{-\Gamma}, \quad (2.45)$$

so, using  $\Delta E_e / \Delta E_i = g_{lp}^{-1}$  and  $\Delta t_e / \Delta t_i = g_{lp}$ ,

$$N_i \sim \left( \frac{g_{lp}}{E_i} \right)^\Gamma. \quad (2.46)$$

Combining all this, the total incident flux on the accretion disc is:

$$F(r) \sim \frac{\sin \alpha g_{lp}^\Gamma}{A(r, \Delta r, \theta) \gamma^{(\phi)}}. \quad (2.47)$$

## 2.4 ENERGY SHIFTS

Getting information about the black hole system is often based on the investigation of emission lines in the observed spectra. These lines are broadened and shifted in their energy when they reach the observer. The underlying mechanisms are the gravitational redshift and the Doppler shift, which are presented here.

### 2.4.1 GRAVITATIONAL ENERGY SHIFT

Assume a photon is emitted at radius  $r_e$  and detected by a distant, stationary observer. Then the measured energy is given by

$$E = -p \cdot u, \quad (2.48)$$

where  $u$  is the 4-velocity of the observer and  $p$  the photon's 4-momentum. Since the observer is stationary, the only non-vanishing component of  $u$  is the time component  $u^0$ , which can be determined by the normalization of the 4-velocity, which then reads:

$$u \cdot u = g_{\mu\nu} \frac{dx^\mu}{d\tau} \frac{dx^\nu}{d\tau} = g_{00} u^0 u^0 = -1. \quad (2.49)$$

Therefore

$$u^0(r) = \sqrt{\frac{-1}{g_{00}}} = \left(1 - \frac{r_s}{r}\right)^{-1/2}. \quad (2.50)$$

Using the Killing vector (2.8), we can express  $u$  as

$$u^\mu = \left(1 - \frac{r_s}{r}\right)^{-1/2} \xi^\mu, \quad (2.51)$$

---

<sup>2</sup>it can be substituted with the exact expression for the energy shift for surface elements off the equatorial plane, derived later for the Schwarzschild case

and consequently

$$E = -p \cdot u = -\left(1 - \frac{r_s}{r}\right)^{-1/2} (\xi \cdot p). \quad (2.52)$$

But since  $\xi$  is a Killing vector,  $\xi \cdot p$  is conserved along geodesics, i.e. independent of  $r$ . Thus the emitted energy  $E_e$  and the energy measured by the observer ( $r \rightarrow \infty$ ) can be expressed as

$$\begin{aligned} E_e &= -\left(1 - \frac{r_s}{r_e}\right)^{-1/2} (\xi \cdot p) \\ E &= -(\xi \cdot p), \end{aligned} \quad (2.53)$$

so the gravitational energy shift is given by

$$g_{\text{grav}} \equiv \frac{E}{E_e} = \sqrt{1 - \frac{r_s}{r_e}}. \quad (2.54)$$

Analogously, the expression for an emitter at  $r_1$  and the receiver at  $r_2$  is:

$$g_{\text{grav}} \equiv \frac{E_2}{E_1} = \sqrt{\frac{1 - \frac{r_s}{r_1}}{1 - \frac{r_s}{r_2}}}. \quad (2.55)$$

### 2.4.2 DOPPLER SHIFT AND ABBERATION

In addition to the gravitational energy shift there is another one, the Doppler shift, due to the rotation of the disc with respect to the stationary observer. Its magnitude depends on the velocity of the source  $v$ , in this case given by (2.39), and the angle  $\rho$  between the direction of motion and the normalized initial direction of the photon when emitted  $\mathbf{k}_0$ :

$$\cos \rho = \frac{\mathbf{v} \cdot \mathbf{k}_0}{v}. \quad (2.56)$$

$\mathbf{k}_0$  is obtained by solving equation (2.19), where  $\phi$  is the projection of the inclination vector  $\mathbf{i}$  projected into the plane of the trajectory. The Doppler factor then is

$$\delta = \frac{1}{\gamma(1 - v \cos \rho)}, \quad (2.57)$$

with the usual Lorentz factor  $\gamma$ . This Doppler factor is also needed as normalization for Lorentz transformations: Introducing an instantaneous non-rotating cartesian coordinate system at any time, such that the y-axis is directed along the 3-velocity of the emitting surface element and the z-axis along the position vector  $\mathbf{r}$ , means that  $\mathbf{k}_0$  in these coordinates is given by (Poutanen & Beloborodov, 2006)

$$\mathbf{k}_0 = \begin{pmatrix} k_{0,x} \\ \cos \rho \\ \cos \alpha \end{pmatrix}. \quad (2.58)$$

The expression for  $k_{0,x}$  can be given explicitly, but has no further meaning. In the frame rotating with the disc (still y-axis along velocity direction, z-axis along  $\mathbf{r}$ ) the initial photon direction is then given by the Lorentz transformation

$$\mathbf{k}'_0 = \delta \begin{pmatrix} k_{0,x} \\ \gamma(\cos \rho - v) \\ \cos \alpha \end{pmatrix}. \quad (2.59)$$

The z-components of the last two formulae combined describe the aberration of light rays (Poutanen & Beloborodov, 2006):

$$\cos \alpha' = \delta \cos \alpha, \quad (2.60)$$

the emission of photons is focused along the direction of motion.

With the results from the last two subsections  $g_{lp}$  from (2.43) can now be given in the Schwarzschild solution,

$$g_{lp} = \gamma \sqrt{\frac{1 - \frac{r_s}{h}}{1 - \frac{r_s}{r}}}, \quad (2.61)$$

as a combination of gravitational and Doppler energy shifts.

## 2.5 OBSERVED FLUX

This whole section follows Poutanen & Beloborodov (2006). The observed flux from a spot with photon energy  $E$  is

$$dF_E = I_E d\Omega, \quad (2.62)$$

where  $I_E$  is the specific intensity at infinity and  $d\Omega$  is the solid angle of the surface element. The latter can be expressed as

$$d\Omega = \cos \zeta \frac{dS}{D^2} \quad (2.63)$$

with the angle between the spot normal and the photon's momentum at emission  $\zeta$  and the area of the spot  $dS$ , measured in the observers frame an connected to the corresponding quantities in the rest frame of the accretion disc via a Lorentz transformation.  $D$  is the distance to the source, which is assumed to be just a constant, since its magnitude exceeds any distance within the disc by far.

A relation between the the observed and emitted intensities can be obtained as a consequence of the conservation of volume in phase space, as stated by Liouville's theorem. While different observers will measure different energies and specific intensities, the ratio

$$\frac{I_E}{E^3} \quad (2.64)$$

is conserved along a photon's world line. Thus the observed intensity expressed in term of the emitted intensity and the corresponding energies is (primed quantities belong to the co-rotating disc-system as before)

$$I_E = \left(\frac{E}{E'}\right)^3 I'_{E'}. \quad (2.65)$$

$E/E'$  is the overall energy shift  $g \equiv \delta \cdot g_{grav}$ . So the observed spectral flux is given by

$$dF_E = I'_{E'} g^3 \cos \zeta \frac{dS}{D^2}. \quad (2.66)$$

### 2.5.1 VISIBILITY

Unlike for flat accretion discs, where the whole disc is visible for the observer, spots on a flared disc have two conditions to be seen at infinity. Firstly, the geodesics starting on them and leading to the observer may not cross the disc, as it is assumed to be optically thick. This can be tested by the same ray tracing methods used for the irradiation. Secondly the angle between

the tangent of the surface element and its position vector has to be smaller than the angle between the latter and the initial direction of the photon, in order to leave the disc at all. This second condition is easy to test, as all needed quantities can be easily calculated, using the derivative of (2.1) and previously obtained results as in section 2.4.2 described.

For the purpose of illustration, the projection of the single surface elements on the observers plane of sky is a nice thing to have. Centered around the line of sight with  $A$  being the projected y-component and  $B$  the projected x-component of such a surface element is given by (see Falkner et al., 2013):

$$\begin{aligned}
 A &= \frac{\sin \theta \sin \phi}{\sqrt{\sin^2 \theta \sin^2 \phi + (\sin i \cos \theta - \cos i \sin \theta \cos \phi)^2}} b \\
 B &= \frac{\sin i \cos \theta - \cos i \sin \theta \cos \phi}{\sqrt{\sin^2 \theta \sin^2 \phi + (\sin i \cos \theta - \cos i \sin \theta \cos \phi)^2}} b.
 \end{aligned}
 \tag{2.67}$$

---

## CHAPTER 3

# SIMULATION AND RESULTS

---

The core of this thesis is a simulation of a system consisting of the black hole, the primary source, and the accretion disc. It is based on the theory described in chapter 2. The procedure can be divided into three parts: computing the irradiation of the disc, modeling the disc with a grid of surface elements, each with its own set of parameter (such as flux, redshift, ...) and, at last, calculation of the quantities that can actually be observed: spectra and time lags. The goal is to constrain parameters of the system by looking at these observables. This means looking for signatures of these parameters in the energy and time curves.

For all the simulations the mass of the black hole is set to  $10^6 M_\odot$ . Even though the mass is the quantity that defines the entire spacetime, it just gives a scale for all magnitudes. As it is proportional to the Schwarzschild radius which is a natural length scale in the black hole system, it is also proportional to time (linked via the speed of light). So all the obtained results are qualitatively right for any given mass of the black hole, the scales simply have to be adjusted appropriately. The photon index  $\Gamma$  is always assumed to be 2.

### 3.1 IRRADIATION OF THE ACCRETION DISC

In order to calculate the coordinates where a photon hits the accretion disc, basically the integral (2.19) has to be solved in order to iteratively get the intersection with the disc. The integrand diverges at the periastron, but as it goes to infinity like an inverse square root, this can be handled with the right substitutions.

Given the distance between the impact points of the photons the geometric contribution to the flux illuminating the accretion disc<sup>1</sup> can be calculated, following the procedure in section 2.3. The effects of the Doppler contraction and the curvature of space time on the proper area in the disc frame are illustrated in Fig. 3.1. As expected, they are strongest in the highly relativistic regime at small radii. At distances more than about  $10r_s$  from the singularity the deviations become small. This can be understood evaluating the  $g_{rr}$  element of the metric which is directly linked to the gravitational extension. At  $r = 10r_s$  it is roughly 1.05, so the difference to flat space is just about 5%. The Doppler extension (or contraction) is determined by the velocity of the disc, which is shown in Fig. 3.2. It is plotted for different spin values, given in percent of the maximal spin a black hole can have. This limit coincides with the mass of the black hole, though a realistic upper limit is given by  $0.998M$  (see Thorne, 1974). For the non-rotating black hole assumed here the velocity of the disc approximately halves from  $\sim 0.5c$

---

<sup>1</sup>The shape of the disc is not limited to the one defined in Eq. (2.1). The irradiation of a neutron star for example is already part of the simulation, other geometries can be implemented easily.

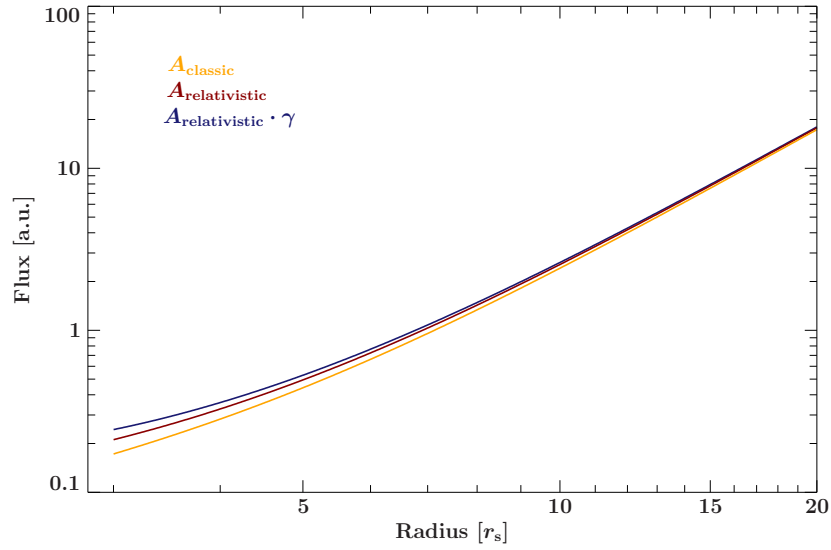


Fig. 3.1: The effect of gravitational and Doppler corrections to the area of annuli of the accretion disc. The calculation was performed for zero spin. The effects are clearly stronger in the highly relativistic regime near the black hole.

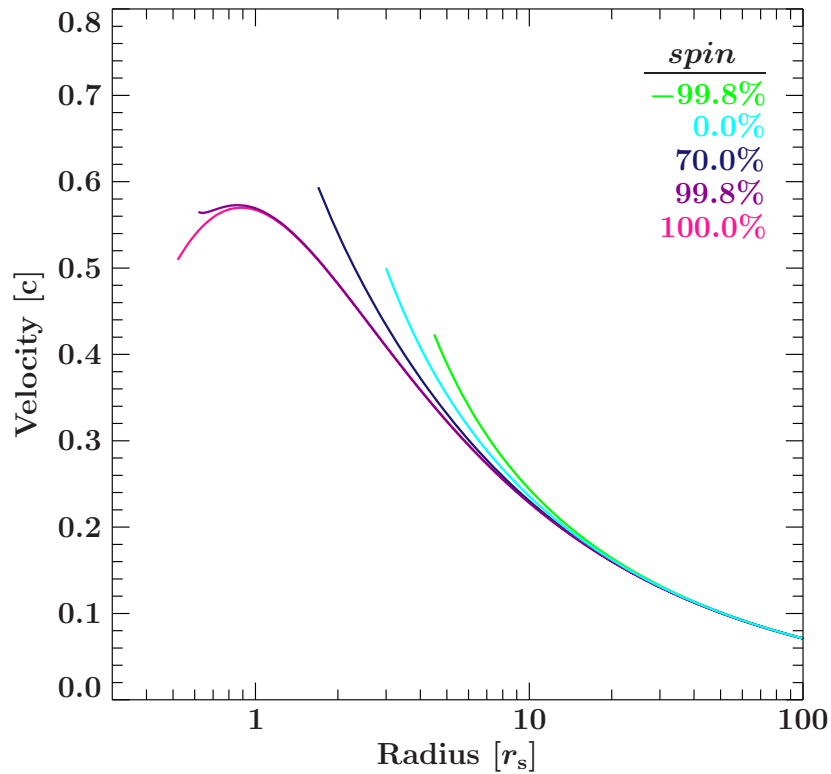


Fig. 3.2: Velocity profiles for accretion discs of black holes with different spins. The cut-off at small radii corresponds to the inner edge of the discs, which is related to the spin. Note that the dependency from the radius is not monotone for high spin.

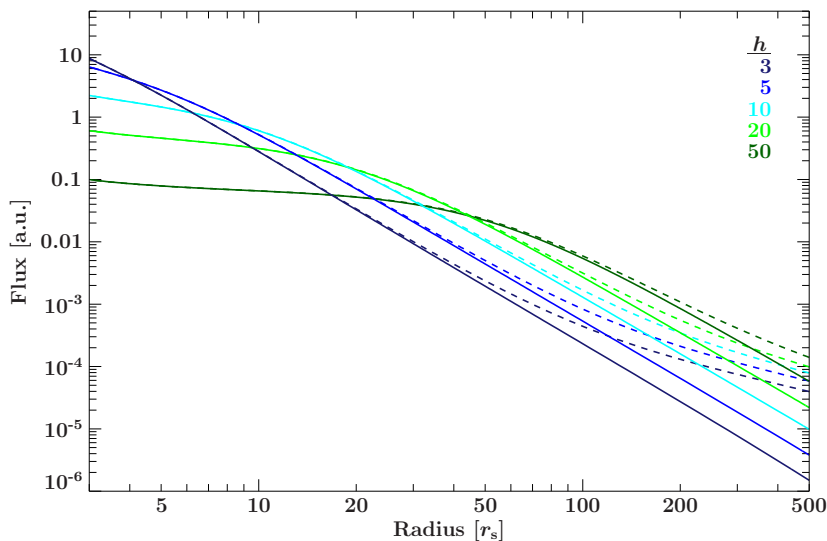


Fig. 3.3: Flux illuminating the accretion disc for different heights  $h$  (in  $r_s$ ) of the primary source. The solid lines represent a flat disc in the equatorial plane, the dashed lines a flared disc with  $\xi = 2.0$ ,  $r_{\text{out}} = 10^3 r_s$  and  $H/r_{\text{out}} = 0.3$ . For lower heights of the source the radiation is collimated to the inner regions of the disc. Only for the outer region the warped disc deviates significantly from the flat one, resulting in a higher flux there.

at the inner edge of the disc to  $\sim 0.25c$  at  $r = 10r_s$ , explaining the drop in the Lorentz factor. One interesting fact worth mentioning, though not relevant for this work, is that the velocity profile for high spin is not monotone, so the velocity of the disc is not maximal for the smallest radii. Furthermore, for a given  $r$ , the velocity is higher for an accretion disc of a non-rotating black hole than for one with maximal spin.

Including the effects of energy shifts and dependency of the emission angle, the flux at the surface of the disc, given by Eq. (2.47), is shown in Fig. 3.3 for different source heights. The solid line represents a flat disc, the dashed line a flared one with  $\zeta = 2.0$ ,  $r_{\text{out}} = 1000r_s$  and  $H/r_{\text{out}} = 0.3$ . For lower heights  $h$  the flux at the inner region of the disc is significantly higher than for bigger radii, due to the strong light bending near the center of mass. This effect becomes weaker as  $h$  increases, so the outer region becomes more important. The increasing height of the flared disc has the same effect. Since the effective area gets bigger for larger  $r$  (the surface ‘turns towards the source’) the flux increases. It has to be mentioned, that the choice of the photon index strongly influences the flux for smaller radii (Dauser et al., 2013), which is nevertheless not further followed up in this thesis.

The easiest models for the disc illumination assume the flux on the surface of the disc to be given by a power-law with constant index 3, i.e.,  $F \sim r^{-3}$  (e.g., Laor, 1991). To compare this assumption with the results obtained here, Fig. 3.4 again shows the flux of the flared accretion disc, this time scaled with the third power of the radius  $r$ . For a constant power-law index of 3 these curves should be constant. This is roughly the case for radii about twice as large as the height of the source. In contrast, for the inner region we see a steep slope, which means that the power-law index in this case is bigger than assumed. This again reflects the focusing of the radiation towards the black hole.

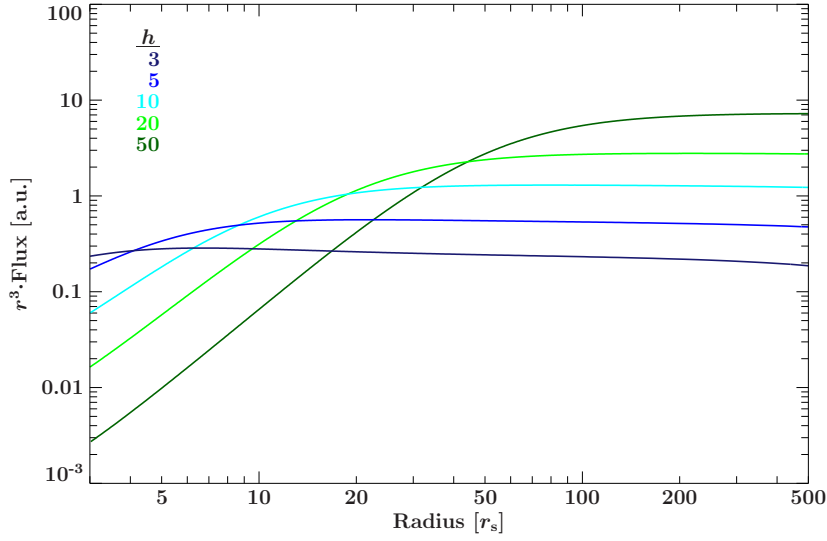


Fig. 3.4: Flux with the same parameters as in figure 3.3, but multiplied with  $r^3$ . This plot shows the difference to the power-law emissivity in the standard model with power-law index 3, which holds only for the parts of the disc with more or less big radii, depending of the height of the primary source. In the inner region of the disc emissivity profile is a lot steeper, due to the collimation of the radiation by light bending.

### 3.1.1 FLUX OF AN ANISOTROPIC SOURCE

These results so far were obtained for an isotropic, spherical source. As mentioned before, sources with other radiation characteristics are worth of consideration. The emission of a plasma bulk at a certain height is given by Eq. (2.42). Based on that, integrating over an interval of heights one could simulate the base of a jet as primary source. The change in the incident flux of the accretion disc is shown in Fig. 3.5. For the bulk velocity directed towards the black hole the illumination of the inner region gets stronger. This can again be explained (besides the generally different angle dependency) by aberration effects as derived in section 2.4.2: the radiating medium is moving in direction of the black hole, so the light is beamed in this direction and thus amplifying the effect of the light bending. The effect is weaker for smaller heights, but this is relative, since in that case the radiation is already focused stronger than for higher sources. For the source moving away from the singularity, the beaming due to the motion of the source and the light bending due to the curved spacetime counteract, so the overall effect is weaker. The result is a lower flux at small radii for small heights of the source and an increase in flux for bigger  $h$ .

## 3.2 RADIATION TRANSPORT FROM DISC TO OBSERVER

In order to calculate the time delay of a particular disc segment as well as for the Doppler shift and the flux measured by the observer, we need knowledge of the angle, under which a photon has to be initially sent out from the accretion disc. As discussed before, the photon's trajectory lies in a plane. It is defined by the position of the singularity (the center of the black hole), the position where the radiation is emitted and, as the photon shall reach the observer, the

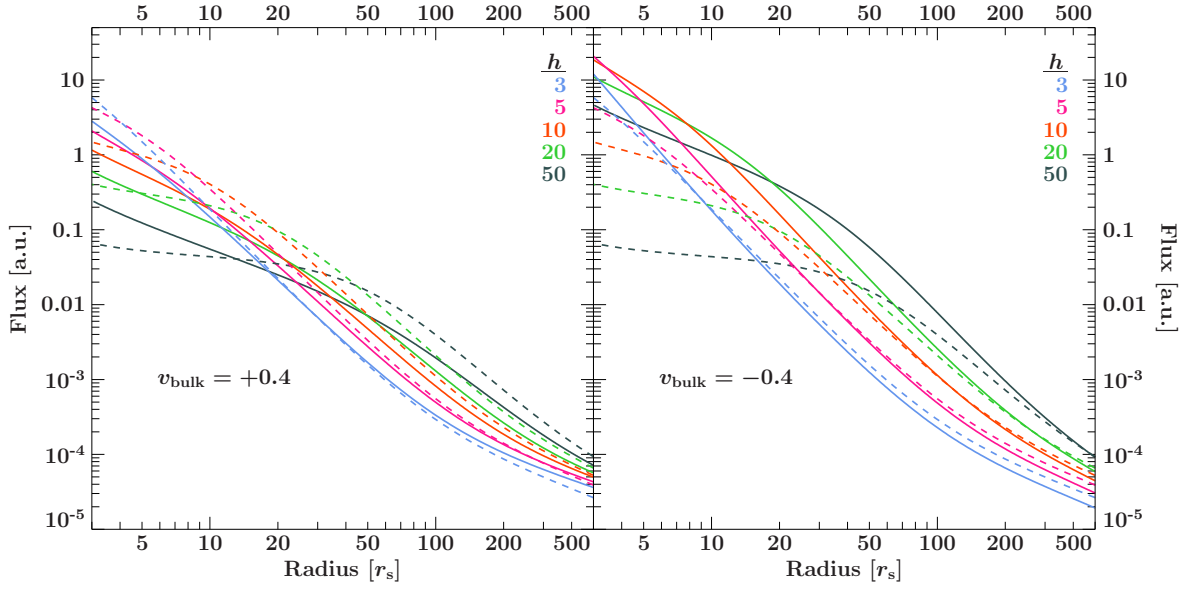


Fig. 3.5: This plot also shows the irradiation of a flared accretion disc with the same parameters as in figure 3.3 (dashed lines), but this time compared with the anisotropic irradiation (solid lines) of a source moving away from the black hole with a bulk velocity of  $0.4c$  (left panel) and towards the black hole (right panel) as described in (2.42).

inclination vector. So this angle is calculated by solving the integral equation

$$\int_{r_e}^{\infty} \frac{dr}{r^2} \left[ \frac{1}{b^2} - \frac{1}{r^2} \left( 1 - \frac{r_s}{r} \right) \right]^{-1/2} = \varepsilon, \quad (3.1)$$

where  $\varepsilon$  is the angle between the radial direction and the projection of the inclination vector into the plane.  $r_e$  is the radius of the emission point. The dependency of the emission angle is in the impact parameter  $b$ , compare Eq. (2.31). In case the periastron (at radius  $r_p$ ) lies on the photon's way to the observer, the integral has to be split:

$$\int_{r_p}^{r_e} \frac{dr}{r^2} \left[ \frac{1}{b^2} - \frac{1}{r^2} \left( 1 - \frac{r_s}{r} \right) \right]^{-1/2} + \int_{r_p}^{\infty} \frac{dr}{r^2} \left[ \frac{1}{b^2} - \frac{1}{r^2} \left( 1 - \frac{r_s}{r} \right) \right]^{-1/2} = \varepsilon. \quad (3.2)$$

This case differentiation has to be done for every integration over  $r$  appearing in the work, so from now it is assumed to be implicitly. Since the photons travel with the speed of light, which is independent of the reference frame, the travel time does not depend on any relative motion of the accretion disc with respect to the observer. This means that the integral equation can be solved in the observer's rest frame.

However, the direction of emission in the co-rotating disc frame can be of interest, say for the case of anisotropic emission. It is obtained by a Lorentz transformation, see Eq. (2.60). Figure 3.6 shows a map of the emission angle in the disc frame, the disc is projected as it would be seen by a distant observer. Again, the parameters describing the accretion disc are  $\xi = 2.0$ ,  $r_{\text{out}} = 1000r_s$  and  $H/r_{\text{out}} = 0.3$ . The projection is obtained using (2.67), the necessary impact parameter can be calculated using  $\varepsilon$ . The inclinations of the system are  $70^\circ$  for the left panel and  $30^\circ$  for the right one. The asymmetries are due to the aberration, the photons are 'beamed' in the direction of the disc's motion, the left part of the disc moves towards the observer, the right part away from her. Furthermore, for the higher inclination another effect

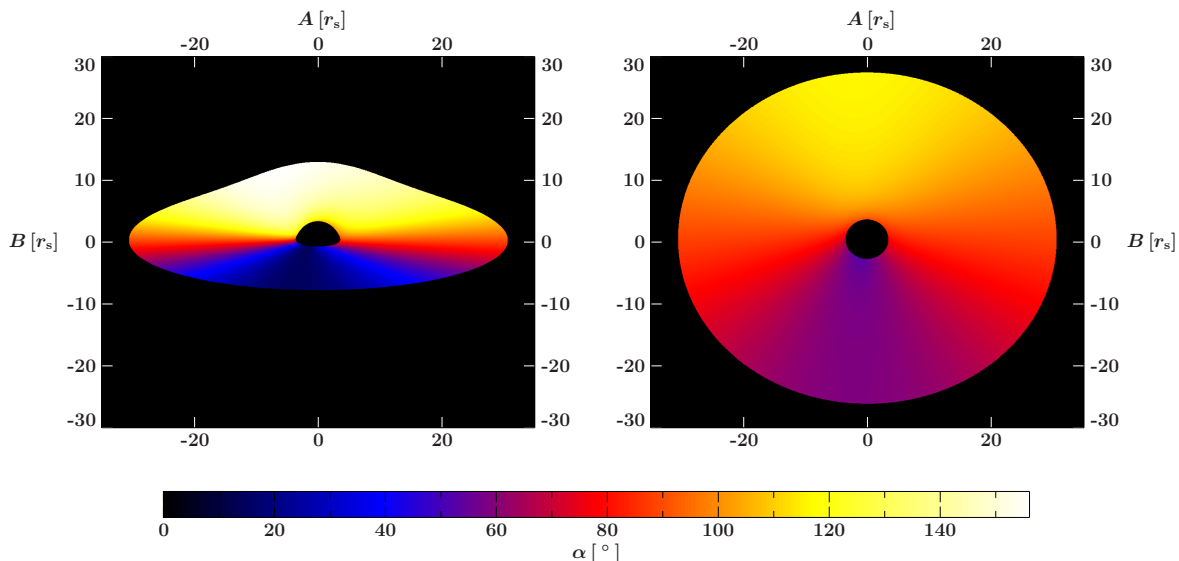


Fig. 3.6: Accretion disc as it would be seen by a distant observer, in the left panel under an inclination of  $70^\circ$  and  $30^\circ$  for the right panel. The color code represents the angle between the radial direction and the initial direction of the photons when leaving the disc. The slight asymmetries are due to the aberration described in section 2.4.2.

of light bending is clearly visible: the part of the disc lying behind the black hole appears to be fold up, a consequence of the light passing by the black hole.

The simulation providing the data for the presented results was coded in C, using several of the numerical methods, or algorithms based on them, presented by Press et al. (1992). The maximal tolerated truncation error for solving integrals and root finding was set to  $10^{-12}$  (in  $r_s$ ). According to gprof<sup>2</sup>, the number of calls of the corresponding functions does not exceed several hundreds per obtained final result. So the accuracy of the model is reasonable high.

### 3.3 CALCULATING TIME LAGS AND EMISSION LINE SPECTRA

The next step is the calculation of iron lines and time lags. The required information is carried by the photons, each and every provided with its own energy and time delay. The energy with which it arrives at the observer is easy to obtain, it is the energy it was released with at the accretion disc (e.g., 6.4keV for the  $K_\alpha$  iron line) multiplied with the total energy shift  $g$ . Calculating the observed spectrum means integrating the differential spectral flux  $dF_E$ , Eq. (2.66), over the whole accretion disc for every occurring energy. In order to do so the distance  $D$  from the observer to the emitting spot at the disc is assumed to be the same for every surface element. This is justified, since in our model the observer sits at infinity so the extent of the disc itself is negligible compared to  $D$ , which then is just a constant.

The time lag  $\Delta t$  is the difference of the travel time of the reflected radiation, i.e., from the source to the accretion disc and from there to the observer, and the travel time of radiation

<sup>2</sup>[http://www.cs.utah.edu/dept/old/texinfo/as/gprof\\_toc.html](http://www.cs.utah.edu/dept/old/texinfo/as/gprof_toc.html)

reaching the observer directly from the source:

$$\Delta t = \left| \int_h^{r_i} \frac{dr}{1 - \frac{r_s}{r}} \left[ 1 - \frac{b_1^2}{r^2} \left( 1 - \frac{r_s}{r} \right) \right]^{-1/2} \right| + \int_{r_i}^{\infty} \frac{dr}{1 - \frac{r_s}{r}} \left[ 1 - \frac{b_2^2}{r^2} \left( 1 - \frac{r_s}{r} \right) \right]^{-1/2} - \int_h^{\infty} \frac{dr}{1 - \frac{r_s}{r}} \left[ 1 - \frac{b_3^2}{r^2} \left( 1 - \frac{r_s}{r} \right) \right]^{-1/2}, \quad (3.3)$$

$r_i$  is the radius of the emitting surface element and the  $b_i$  the impact parameters for the different photon trajectories, which depend of the emission angle at their respective source. Of course the last two integrals diverge as traveling an infinite distance takes infinitely long, even with the speed of light. This can be solved in two different ways. In both cases the integrals have to be split first into one part integrated from a common radius  $r_c$  to infinity and the respective rest (that is finite). Then either the difference of the integrands can be integrated, which converges. Or one can introduce a relative time delay with respect to an impact parameter equals zero (Poutanen & Beloborodov, 2006),

$$\delta t_{2,3} = \int_{r_c}^{\infty} \frac{dr}{1 - \frac{r_s}{r}} \left( \left[ 1 - \frac{b_{2,3}^2}{r^2} \left( 1 - \frac{r_s}{r} \right) \right]^{-1/2} - 1 \right), \quad (3.4)$$

which also converge and can then be subtracted. The time delay then gets integrated over the whole accretion disc and for every occurring lag, just like the energy, to obtain the measured time curve. In both cases the obtained flux is the photon flux. If one is interested in the energy flux rather than the photon flux, the differential spectral flux has to be multiplied with the respective measured energy.

Figure 3.7 shows the distribution of the time delay for same disc as in Fig. 3.6, again for inclinations  $\theta$ . The axisymmetry is the result of the universality of the speed of light as explained above.

A main goal of this thesis is the comparison of time lags in curved and flat spacetime. To calculate the time delay in the latter case is easy, it is the distance between the source and the point where the photon hits the disc minus the projection of the position vector of this spot,  $\mathbf{r}$ , on the inclination vector  $\mathbf{i}$ , which is given by  $\mathbf{r} \cdot \mathbf{i}$ . Figure 3.8 shows a map of the ratio of the general relativistic time delay and classical equivalent. The values for the ratio are highest at the inner edge of the disc. This is reasonable, since the light bending is strongest there and thus also the deviation of the world line of the photon from a straight line. The further away from the center of mass the closer the ratio gets to 1, reflecting the fact that far away from the black hole the spacetime becomes asymptotically flat.

### 3.4 THE OBSERVED FLUX

In order to understand the emission lines and time lags some knowledge of the observed flux is needed. Recall the differential spectral flux:

$$dF_E = I'_{E'} g^3 \cos \zeta \frac{dS}{D^2}. \quad (2.66)$$

The intensity  $I$  is to identify with the incident flux described in section 3.1. The assumption behind this is that the intensity the accretion disc emits with is proportional to the intensity

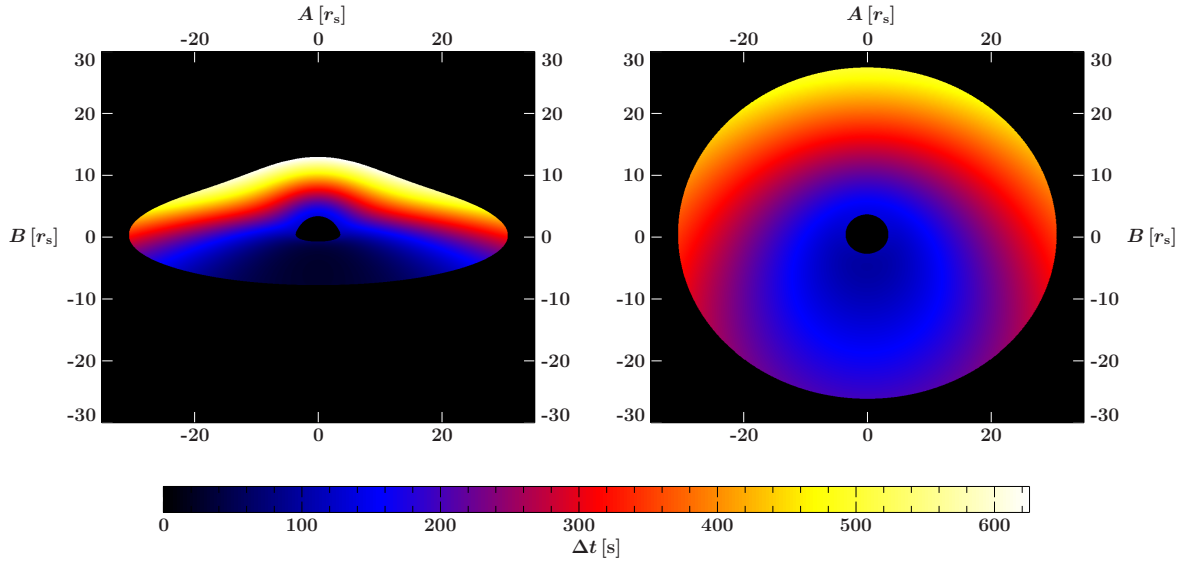


Fig. 3.7: Distribution of the time delay of the surface elements with respect to the primary source. The inclinations are  $70^\circ$  in the left panel and  $30^\circ$  in the right panel. Note that the time delay is independent of the rotation of the disc, a result of the universality of the speed of light.

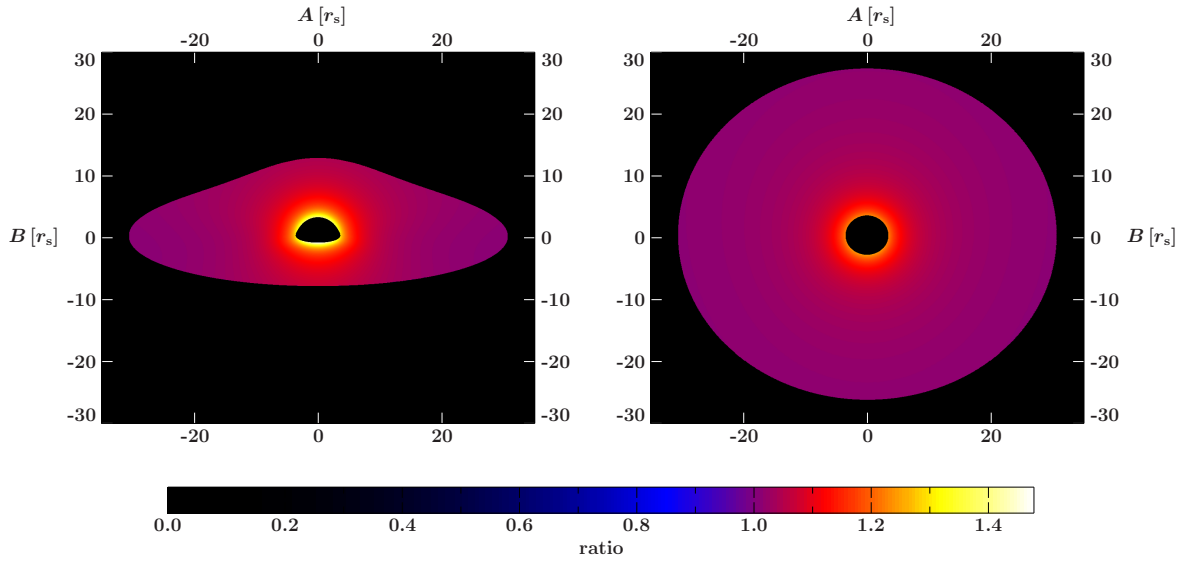


Fig. 3.8: Ratio of the time delay between curved and flat spacetime. As the difference in travel time depends on the deviation of the photon's world line with a straight line to the observer, the ratio is highest where the bending effects are strongest, i.e., near the black hole. The bigger the radius gets, the closer to 1 is the ratio, as spacetime is almost flat far away from the center of mass. Inclinations are as before  $70^\circ$  and  $30^\circ$ .

it is irradiated with. In our model this rate does not vary from one place to another<sup>3</sup>. The differential area  $dS$  is the area of the surface element. It has to be measured in the rest frame of the observer, as well as the projection factor  $\cos\zeta$ . The total energy shift  $g$  is the product of the gravitational redshift and the Doppler shift. The maximal shift in energy increases with

<sup>3</sup>This is of course a simplification. There are physically reasons why it should vary, see later.

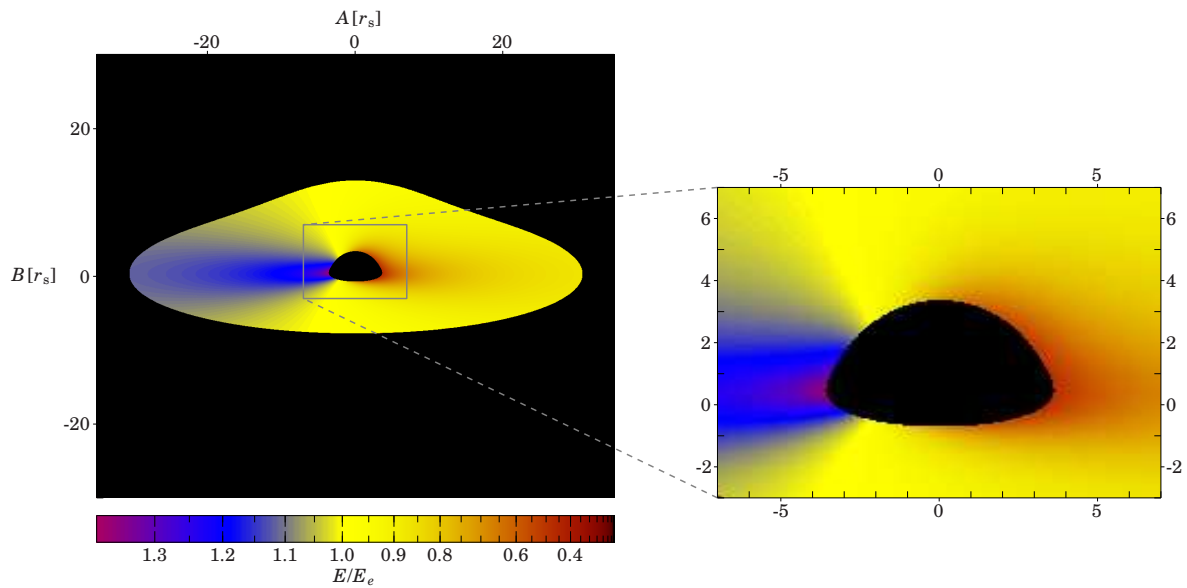


Fig. 3.9: Energy shift map for an accretion disc with spin zero and under an inclination of  $70^\circ$ . The energy shift consists of the gravitational redshift, which is rotationally symmetric and the Doppler shift, depending on the photon's direction of motion with respect to the disc's velocity when leaving the disc. The left, blue shifted part moves towards the observer. As the velocity is highest for small radii (compare figure 3.2), the energy shift is strongest there.

the inclination. While the gravitational redshift depends only on the distance of the emission point to the center of the black hole (compare Eq. 2.54), the Doppler shift scales with the projection of the velocity vector of the disc on the initial photon momentum, which is bigger for higher inclination as the two vectors are stronger aligned for this case (compare Fig. 3.6).

Figure 3.9 shows the red shift for an inclination of  $70^\circ$ . In the left part, moving towards the observer, the photons are blue shifted, up to a factor of about 1.4 closest to the black hole where the disc velocity is highest. This shows that the Doppler shift in principle 'dominates' the gravitational redshift. The redshift on the right side, where the disc moves away from the observer, the energy shift is even stronger. Here both effects cause a shift to lower energies, photons emitted at the inner edge of the disc lose up to 70% of their energy, since both contributions are strongest here.

Finally, Fig. 3.10 shows the flux as it measured by a distant observer, combining all the previous results. The projection factor  $\cos\zeta$  has a different distribution on the disc than the redshift, so multiplying them leads to the asymmetric structure that is seen. The inner region of the accretion disc is distinctly stronger represented than the outer part. But since its area is relatively small compared to the rest of the disc, there are contributions from bigger radii to be expected as well. For higher inclinations the Doppler effect becomes more dominant, so the most luminous parts are shifted more to the left, where the disc moves towards the observer. The flux for lower inclinations is generally higher, because the losses due to projection are smaller in this case.

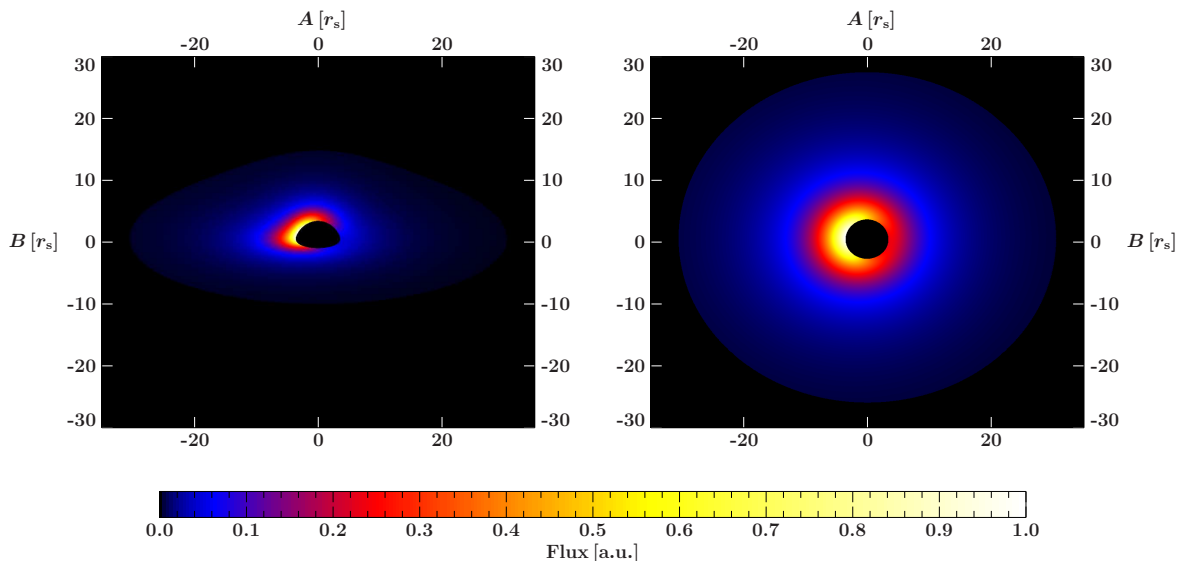


Fig. 3.10: Flux as it reaches the distant observer (Eq. 2.66), as before for inclinations  $70^\circ$  and  $30^\circ$ . It depends on the irradiation of the disc, the redshift and projection factors, resulting in this asymmetric distribution. The overall higher flux for the lower inclination is due to the bigger losses caused by projection for higher inclinations.

### 3.5 TEST OF THE SIMULATION

In order to test the simulation, it is compared with a model that already is approved. The relline model (Dauser et al., 2010) calculates broadened iron lines for flat accretion discs of rotating black holes. So for zero spin and height of the disc ( $H = 0$ ) the resulting spectra should be the same. The comparison is shown in Fig. 3.11. The accordance is satisfying, all features of the spectrum are reproduced. For higher inclination there is a slight disagreement in the flux. This seems to be a relativistic effect, as it disappears when a larger inner radius of the disc is chosen. Nevertheless, the small deviations do not affect the validity of the qualitative results.

Even though the flat disc is just a special case of this simulation, this tells that the computation of the irradiation of the accretion disc and the observed flux provide the right results and there is no reason to assume other for the case of a flared disc.

### 3.6 TIME DELAY IN FLAT AND CURVED SPACETIME

The motivation of this thesis was the assumption that considering a curved spacetime instead of a flat one significantly changes the obtained time lags. So before going into a detailed analysis of the impact of the different parameters it shall be shown that there actually are differences between the two cases. Figure 3.12 shows the comparison of time lags for different combinations of inclination and height. The solid line represents the time delay calculated considering all relativistic effects, the dashed line shows the time lag for flat space time. For the latter case that means that only the lag itself is calculated using Euclidean geometry, the underlying flux is the same as for the case in Schwarzschild spacetime. There are some obvious differences. First of all the time delays for the flat space are shifted to lower values. This is an

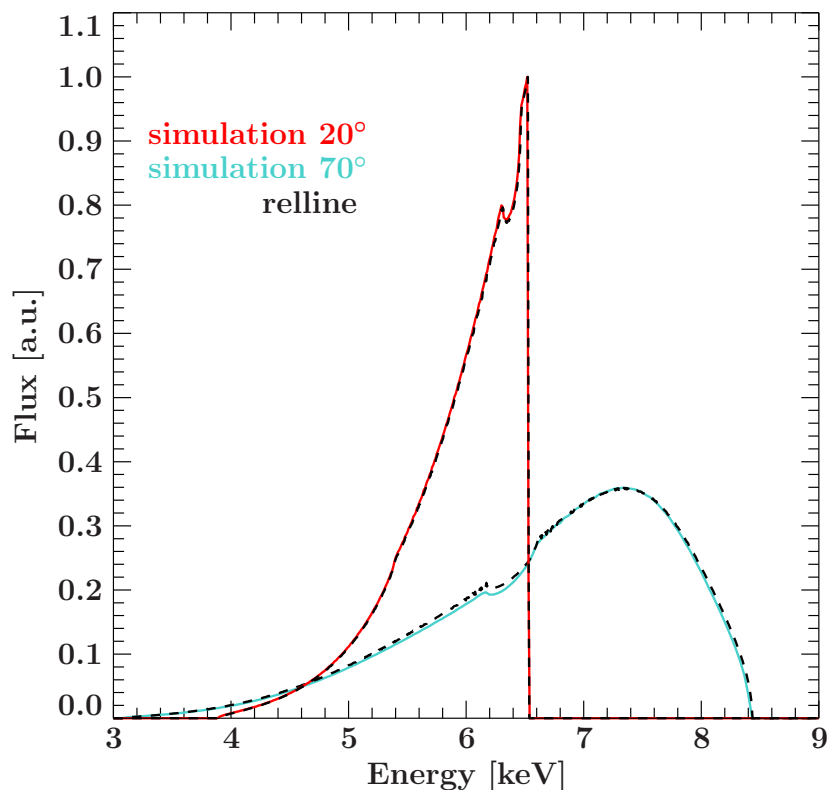


Fig. 3.11: Comparison with the relline model (by Dauser). The graph shows a broadened iron  $K_\alpha$  line, radiated from the disc's surface with an energy of  $6.4\text{keV}$  under inclinations of  $20^\circ$  and  $70^\circ$ . Despite a slight difference in the energy flux the agreement is quite well, every feature of the line can be reproduced. The calculation was performed for a flat disc, zero spin and an outer disc radius of  $400r_s$ .

effect we expect, since the straight line is always the shortest connection between two points<sup>4</sup>, so the travel time is shorter on that path than on any other.

Furthermore, all the time curves happen to have two peaks (even though for big heights of the primary source that almost flatten out). This feature is preserved, but the exact shape is not: the width of the peaks changes, which is relevant for real measurements, because this is a magnitude (beside the position of the peak) that can be evaluated fairly easy from data.

### 3.7 COVERING EFFECTS

On the contrary to the case of a flat accretion disc, where for any inclination the whole disc is visible, in the case of a flared disc the disc can be covered, partly or complete (Section 2.5.1). Figure 3.13 illustrates the covering of the accretion disc for an inclination of  $78.5^\circ$ , a large fraction is hidden to the observer.

This has of course consequences for the measured energy spectra and time lags, which can be seen in Fig. 3.14. For an inclination of  $77^\circ$  the whole disc is visible and thus contributes

<sup>4</sup>Of course in curved spacetime the shortest connection between two points is a geodesic. But in our picture, where the curved space is embedded in the Euclidean flat space it is not. A photon simply can not travel along a straight line, though.

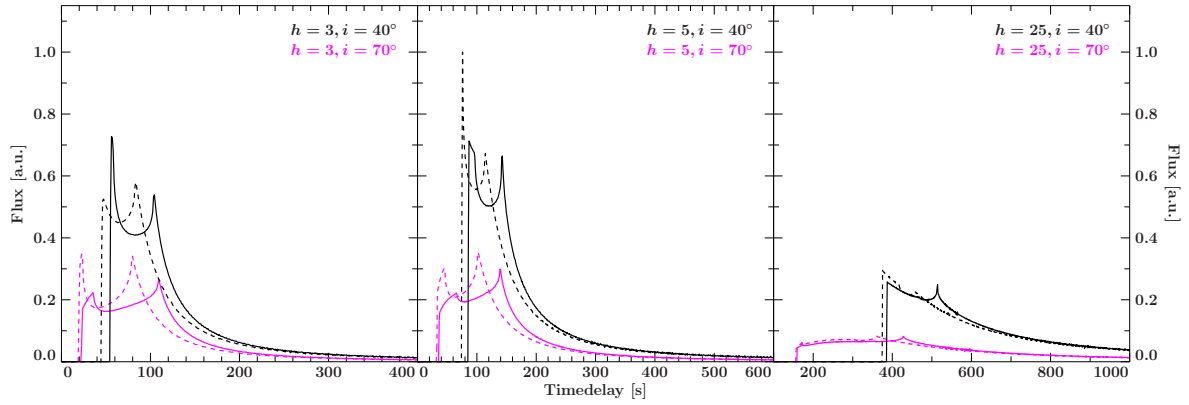


Fig. 3.12: Comparison of the time delay calculated in curved (solid line) and flat (dashed line) spacetime for different inclinations and heights of the primary source. The weight of each disc surface element is the same (relativistic calculation), so the only difference is actually the travel time of the photons. There are obvious differences between the two cases, especially for low heights of the source, which justifies a relativistic treatment of the subject. See text for more details.

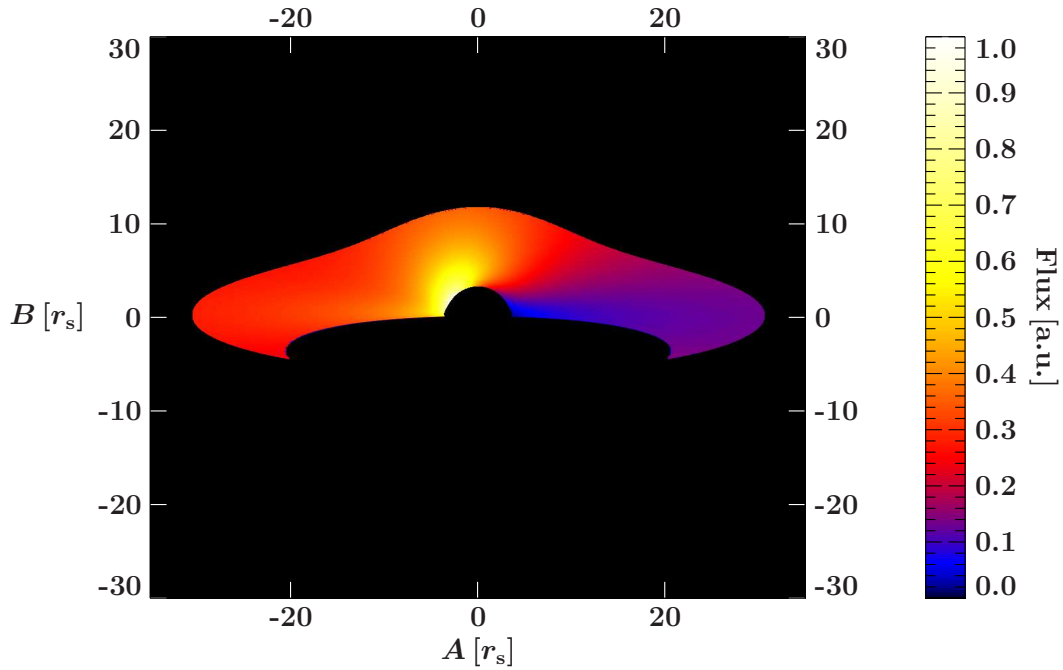


Fig. 3.13: Covering effects of the flared accretion disc: under an inclination of  $78.5^\circ$  a part of the disc covered, as the photons hit the surface again on their way to the observer.

to the measured flux. As the inclination increases, parts of the spectrum and time lag are canceled out, for an inclination of  $80^\circ$  the disc is completely covered by itself.

A detailed analysis of the curves makes no sense, since this discussion would be somewhat idealistic. The exact changes in the spectrum and time delay depend on the shape of the outer edge of the accretion disc. In the simulation it is assumed to follow exactly the definition in Eq. 2.1. This is certainly not the case: for a binary black hole for example the accreted matter

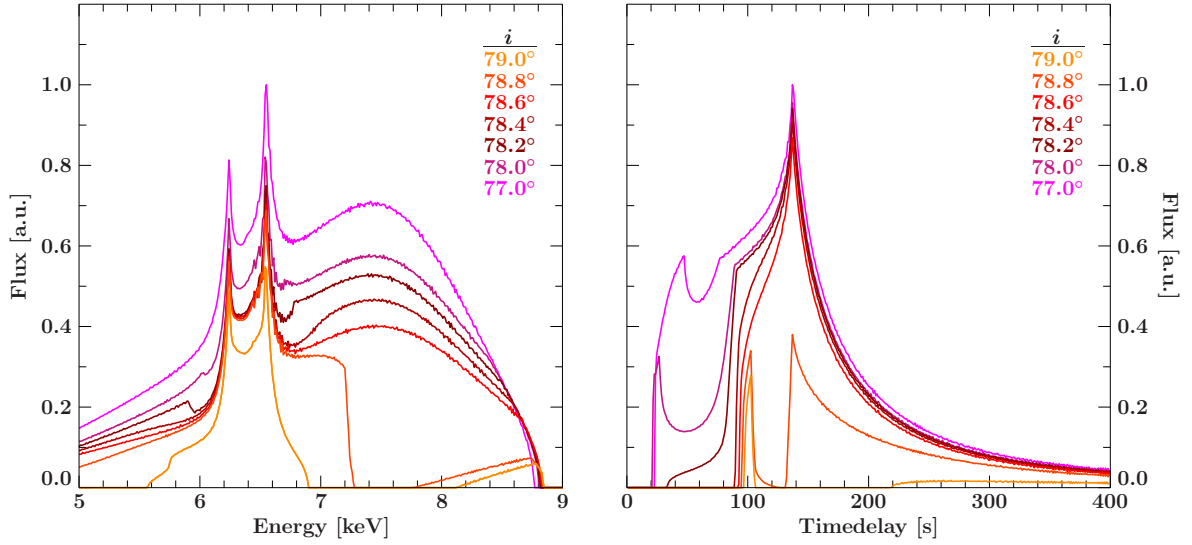


Fig. 3.14: Impact of covering effects on the iron line and the time delay. The window between total coverage and a completely seen accretion disc is with about 2 degrees quite small.

comes from its companion star, so the flow of gas to the disc is not rotationally symmetric but has a preferred direction to the star. Furthermore, the star and the accretion disc revolve around the black hole, so in the outer region it is more likely an ‘accretion spiral’ than an actual disc. So for actual observations this analysis gives more an estimate for which inclinations we do expect to measure flux from a certain region of the disc but an exact shape of emission lines or time lags.

### 3.8 PARAMETER DEPENDENCY OF TIME DELAYS AND BROAD IRON LINES

Recall the definition of the shape of the accretion disc,

$$z(r) = H \left( \frac{r}{r_{\text{out}}} \right)^\zeta. \quad (2.1)$$

In this section we study the effects on the time lags, implied by changes of the parameters of the system. Specifically this means changing the shape of the accretion disc, i.e., the height,  $H$ , and the curvature,  $\zeta$ , the height of the primary source irradiating the disc and the inclination  $i$ . The obtained time delays are compared with the corresponding curves for flat space time. Furthermore, the impact of altering these parameters on measured emission lines (represented by the iron  $K_\alpha$  line) is discussed.

#### 3.8.1 INCLINATION

We start with the inclination. Figure 3.15 shows the broad iron lines for different inclinations. A feature the all spectra share is the prominent double peak. It is caused by the Doppler effect. The red shifted peak originates from the parts of the disc moving away from the observer, the blue shift from the part moving towards her, respectively. The peak at higher energy is

stronger because the flux is proportional to the third power of the energy shift, which is of course higher for the blue shift. This is also the reason for the slope of the ‘continuum’. The Doppler shift does not depend on the velocity of the disc itself but the projection of it on the initial momentum of the photon, which is bigger for higher inclination. This explains why the peaks are further apart the bigger the inclination is. In the case of zero inclination the velocity along the line of sight is zero, so the only energy shift is the gravitational redshift. Thus the two peaks fuse into one single peak (not shown in the figure). The sudden drop in flux at high energies is caused by truncation of the accretion disc at the inner edge, at which the highest blue shift is located. Note that these strong double peaks are a feature of the flared disc, as we shall see later they disappear while transforming it in a flat disc. The decreasing bolometric flux for higher inclinations is, as explained before, due to projection losses.

Figure 3.16 shows the dependence of the time lag on the inclination. The solid lines show the general relativistic time delays. For an inclination of  $80^\circ$  the disc is not visible for the observer (dashed line). In addition there are for comparison the classical time delays for some inclinations (dotted-dashed lines). Just as for the iron line, a double peak structure is visible for all inclinations. But there is no Doppler shift for the time lags! While for the shift of energy there is a direct connection to the observed flux, this is not the case for the time delay. So for the latter the only basis of reasoning is its geometrical distribution and that of the flux. The lags that overlap with the most observed flux are represented strongest in the measured delay.

Comparing the distributions of the flux and the time lags, it follows that the peaks originate from the inner region of the disc (within about  $10r_s$ ). Recalling Fig. 3.7 which showed that at these radii time lags for flat and curved spacetime differ significantly, that means that a general relativistic treatment is indeed necessary. This is reflected in the respective shapes of the lags. The general shift to lower delays for the Euclidean case has been discussed before. For increasing inclinations the left peak of the relativistic lags transforms more and more into a plateau, contrary to the case of flat space. Even more striking is the difference for an inclination of  $10^\circ$ : while for curved spacetime there are two narrow peaks, in Euclidean space there is only broad peak. These differences, especially the last one, are certainly distinguishable in actual observations.

### 3.8.2 HEIGHT OF THE ACCRETION DISC

The next parameter of interest is the height of the accretion disc  $H$ . Increasing it will essentially lead to a higher flux at the outer region of the accretion disc, by orders of magnitudes (compare Fig. 3.3). The question is if this makes any difference, since the flux that far away from the black hole is very low anyways. For the emission lines it does. That is because for big radii the velocity of the disc is relatively small and so is its change with  $r$ . Looking at Eq. (2.57), this implies that Doppler shift does not vary very much as well. The gravitational redshift plays no role for big radii, so out there the overall energy shift is more or less constant. What remains is the  $\phi$ -dependence of the Doppler shift leading to two peaks in the spectrum. So there is a huge area (it scales with  $r$ ) contributing to the spectrum in a small energy range and its size compensates the relatively small flux. Figure 3.17 shows an iron line for different values of  $H$ , the peaks for moderate energy shifts get significantly stronger with increasing height.

For the time lag the situation is different. Its value is determined by the distance a photon has to travel and therefore it scales roughly with  $r$ . This means that unlike the energy shift its variations do not become smaller for large radii. Therefore the flux contributing to a particular

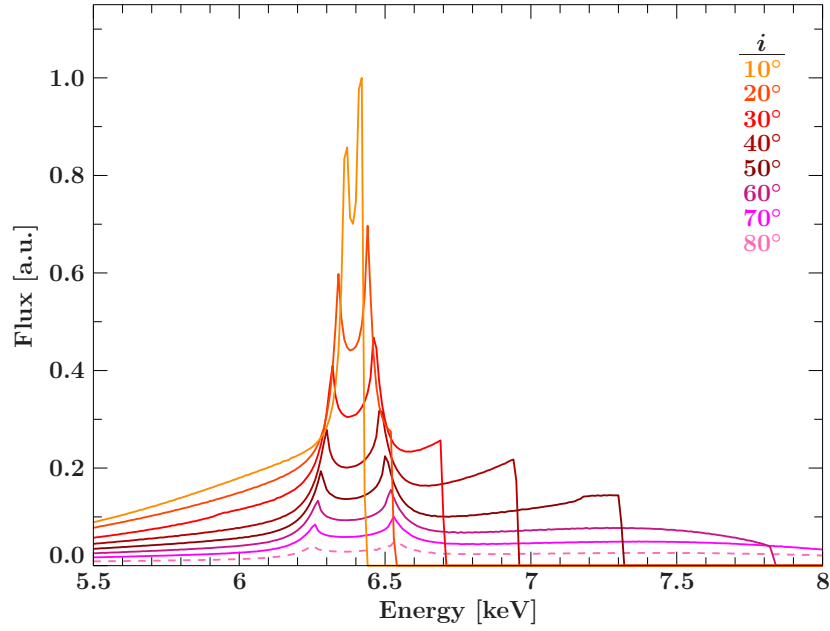


Fig. 3.15: Dependency of the 6.4keV  $K_\alpha$  iron line on the inclination of the system.  $H/r_{\text{out}} = 0.3$ ,  $h = 5r_s$ ,  $\zeta = 2.0$ ,  $r_{\text{out}} = 10^3 r_s$ . The dashed line indicates that the disc is not visible for the observer under this inclination.

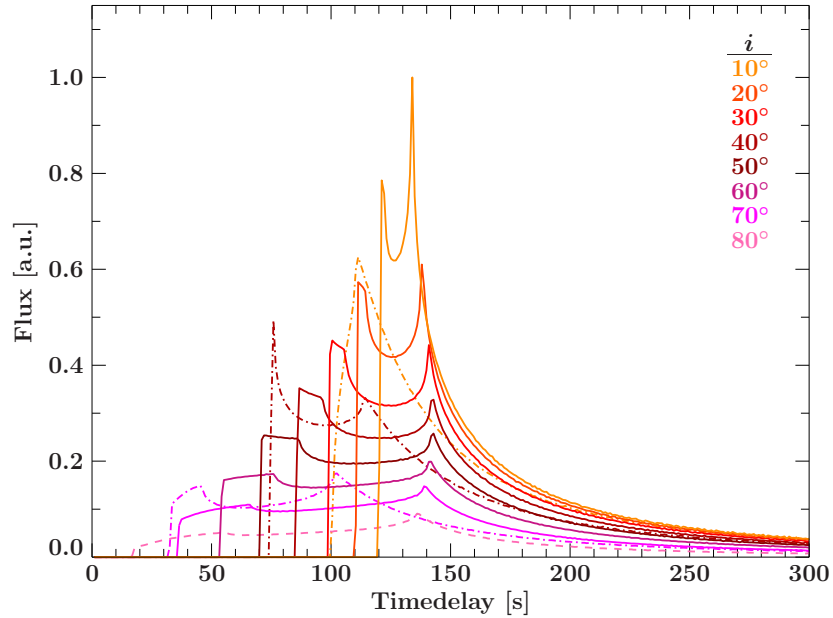


Fig. 3.16: Dependency of the time delay on the inclination of the system.  $H/r_{\text{out}} = 0.3$ ,  $h = 5r_s$ ,  $\zeta = 2.0$ ,  $r_{\text{out}} = 10^3 r_s$ . The time lags for curved spacetime are plotted in solid lines, where the dashed line indicates that the disc is not visible at this inclination. Euclidean time lags are represented by the dashed-dotted lines.

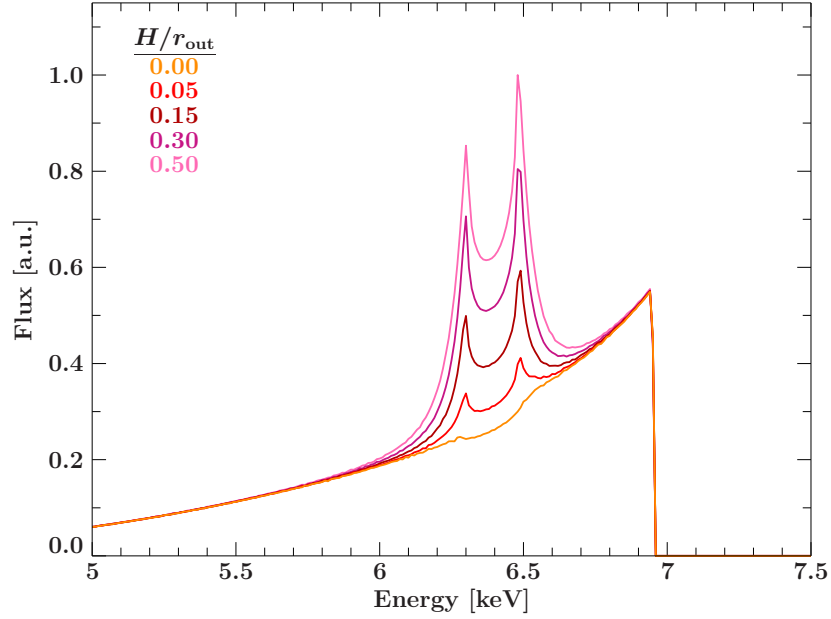


Fig. 3.17: Dependency of the 6.4keV  $K_\alpha$  iron line on the ratio of the maximum height of the accretion disc to the outer radius.  $i = 40^\circ$ ,  $h = 5r_s$ ,  $\zeta = 2.0$ ,  $r_{\text{out}} = 10^3 r_s$ .

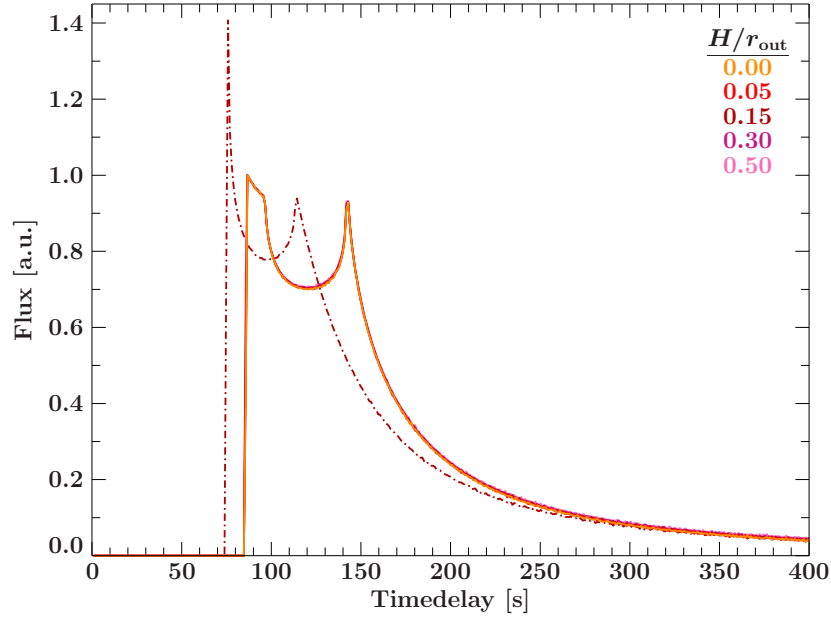


Fig. 3.18: Dependency of the time delay on the ratio of the maximum height of the accretion disc to the outer radius.  $i = 40^\circ$ ,  $h = 5r_s$ ,  $\zeta = 2.0$ ,  $r_{\text{out}} = 10^3 r_s$ . Solid lines represent general relativistic time lags, dashed-dotted lines Euclidean time lags.

delay is very small at regions where changes in the height of the disc alter the flux. So the expectation is that changing  $H$  will not modify the observed time lags. Figure 3.18 shows that that is exactly the case, increasing the height of the disc leaves the time lags unchanged. The same argumentation holds for the Euclidean case, it is not affected as well.

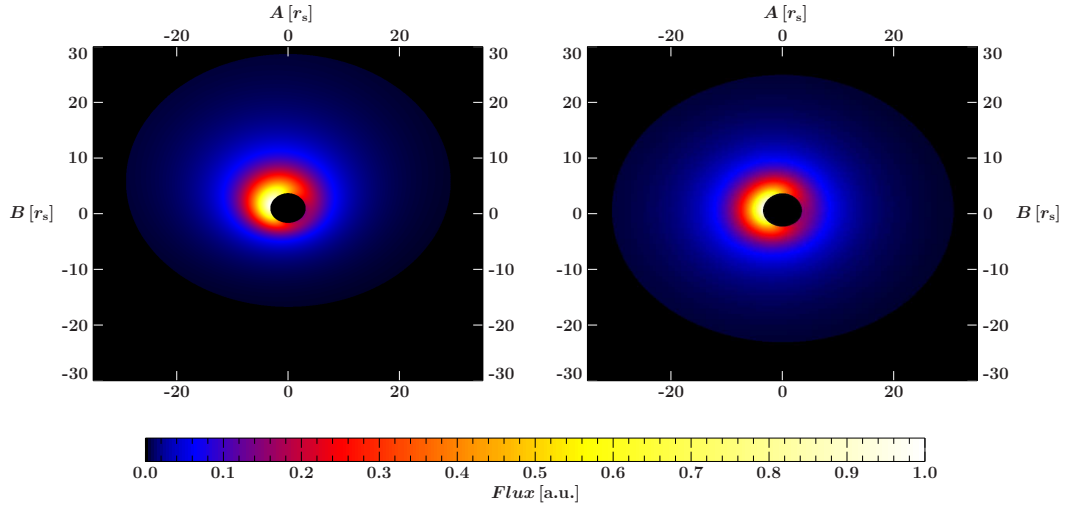


Fig. 3.19: Comparison of the observed flux for same inclination ( $i = 40^\circ$ ) but different power-law indices  $\zeta$ , 1 in the left panel and 2.5 in the right.

### 3.8.3 CURVATURE OF THE ACCRETION DISC

So, does the shape of the disc affect the time delays at all? The second parameter describing the accretion disc is the power-law index  $\zeta$ , which defines its curvature. Changing it results again in a change of flux. But this time the whole disc is affected because the smaller  $\zeta$  gets the more the accretion disc changes at small radii. The effect on the observed flux can be seen in Fig. 3.19. The left panel shows the flux of an accretion disc with  $\zeta = 1$ , i.e., a linear increase of height. So the disc is shaped like a cone. In comparison to the case of  $\zeta = 2.5$  in the right panel, the flux is shifted to the upper half (the half behind the black hole seen from the observer). That is because this half is turned towards the observer and thus its effective area increases. The opposite is the case for the half of the disc closer to the observer. Therefore in the map of the disc the upper half appears bigger. For increasing  $\zeta$  the inner region converges to a flat disc, so no direction is preferred in the projection.

The time lags for different power-law indices are shown in Fig. 3.20. Since for lower  $\zeta$  the origin of the observed flux is focused more on regions further away from the observer, the peak at higher time delay gets stronger and smaller. Furthermore, the curve is shifted to lower delays, because the distance to the source becomes smaller, implying shorter travel times. In addition the first peaks shape changes, for the relativistic time lag as well as for the classical it gets broader.

The change in the energy spectrum of an emission line induced by modifying the curvature of the accretion disc is similar as for changing the the height  $H$  of the disc, which can be seen in Fig. 3.21. Just as described in the case of altering the height, for higher values of  $\zeta$  the outer region of the disc contributes stronger to the spectrum, since it provides more effective area. The result are again two strong peaks for moderate energy shifts. As the slope becomes more constant, the distribution of radiation gets more like that of a flat disc, which means that the flux at large radii decreases, so the peaks get weaker.

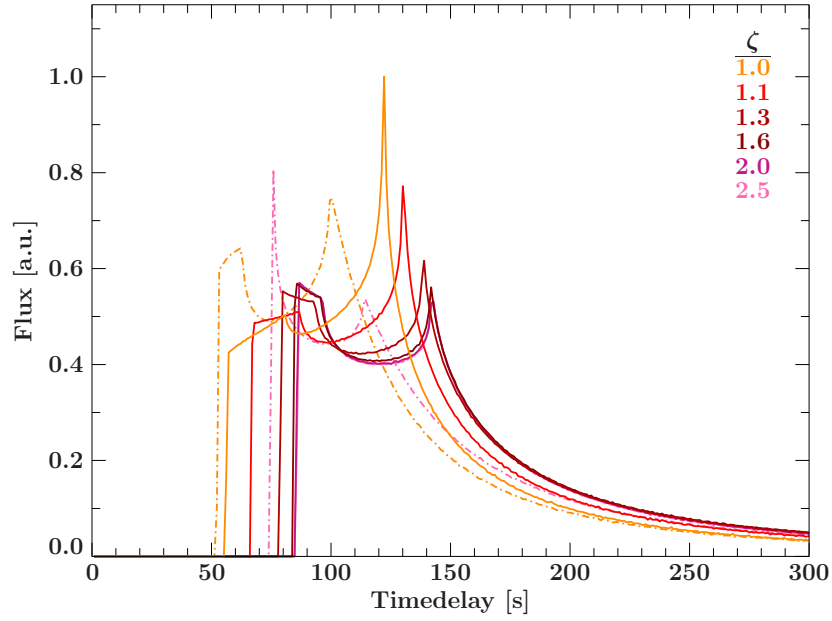


Fig. 3.20: Dependency of the time delay on the curvature of the disc, represented by the power-law index  $\zeta$ .  $H/r_{\text{out}} = 0.3$ ,  $h = 5r_s$ ,  $i = 40^\circ$ ,  $r_{\text{out}} = 10^3 r_s$ . General relativistic time lags are shown in solid lines, Euclidean lags in dashed-dotted lines.

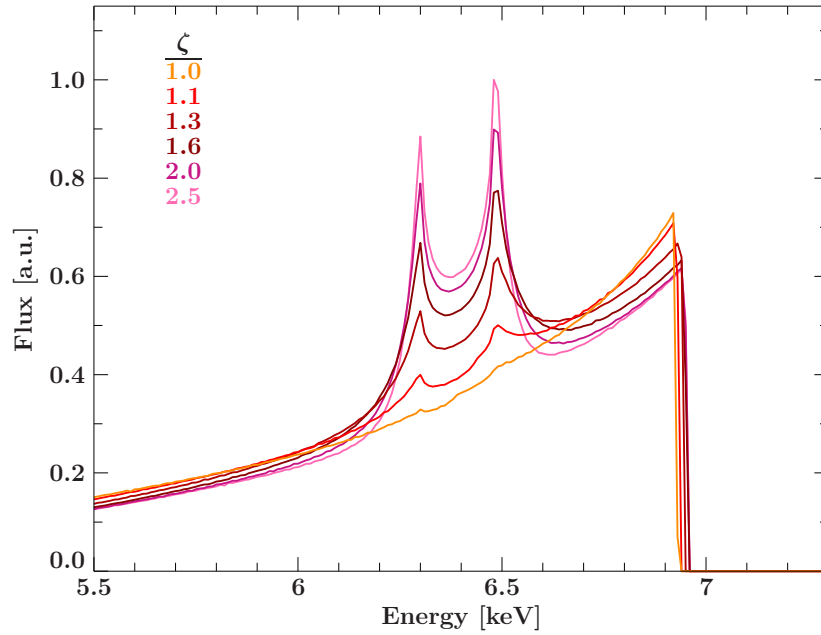


Fig. 3.21: Dependency of the 6.4keV  $K_\alpha$  iron line on the curvature of the disc, represented by the power-law index  $\zeta$ .  $H/r_{\text{out}} = 0.3$ ,  $h = 5r_s$ ,  $i = 40^\circ$ ,  $r_{\text{out}} = 10^3 r_s$ .

### 3.8.4 HEIGHT OF THE PRIMARY SOURCE

The influence of the height  $h$  of the primary source of radiation above the black hole on the incident flux of the accretion disc was discussed in Section 2.3. The main result was that the closer the source is to the black hole the more the radiation is focused to small radii. The

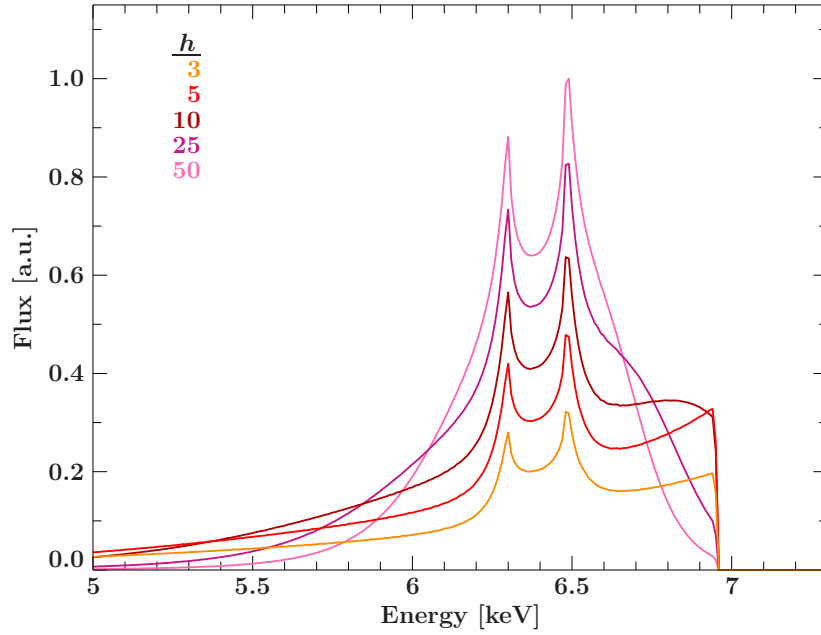


Fig. 3.22: Dependency of the 6.4keV  $K_\alpha$  iron line on the height (in  $r_s$ ) of the primary source.  $H/r_{\text{out}} = 0.3$ ,  $i = 40^\circ$ ,  $\zeta = 2.0$ ,  $r_{\text{out}} = 10^3 r_s$ .

most extreme energy shifts originate from the inner edge of the disc, since the velocity of the disc takes its highest value there (compare Fig. 3.2). This means that for lower sources high energy shifts are measured with higher intensity and with increasing height of the source small energy shifts become stronger. This behavior is shown in Fig. 3.22. For a height of  $3r_s$  we see the already familiar increasing continuum with two peaks from the outer region, for  $h = 50r_s$  the peaks at low energy shifts dominate the spectrum.

The dependence of the time lag on the height  $h$  can be seen in Fig. 3.23. Due to the larger distance from source to accretion disc, the delay is in general higher for bigger  $h$ . One important circumstance is that the difference between the time lags for curved and flat spacetime gets smaller for increasing height. As mentioned before, the region where the delays strongly differ from each other is close to the black hole. So this behavior can be understood, as, like said in the discussion of the emission lines, the irradiation of this region becomes weaker in that case. Furthermore, since the flux is more evenly distributed for larger  $h$ , the peaks get weaker, resulting in a more level curve.

### 3.9 GEOMETRIC ORIGIN OF THE PEAKS IN TIME LAGS

For advanced studies of the accretion disc it can be useful to have knowledge about the regions from where certain features (e.g. the peaks) of the time lags originate from. One motivation for this question is, that, even though assumed for this simulation, the disc is not homogeneous. As described in the introduction, the accreted matter heats up while it approaches the black hole. This may very well lead to different emission characteristics. Looking at the time lag for an inclination of  $i = 30^\circ$  in Fig. 3.16 we see that its two peaks are located at the time intervals 98–108s and 135–145s. Figure 3.24 shows where at the accretion disc these delays come from. Even though for both cases the most of the flux is located near the center, for the larger delay

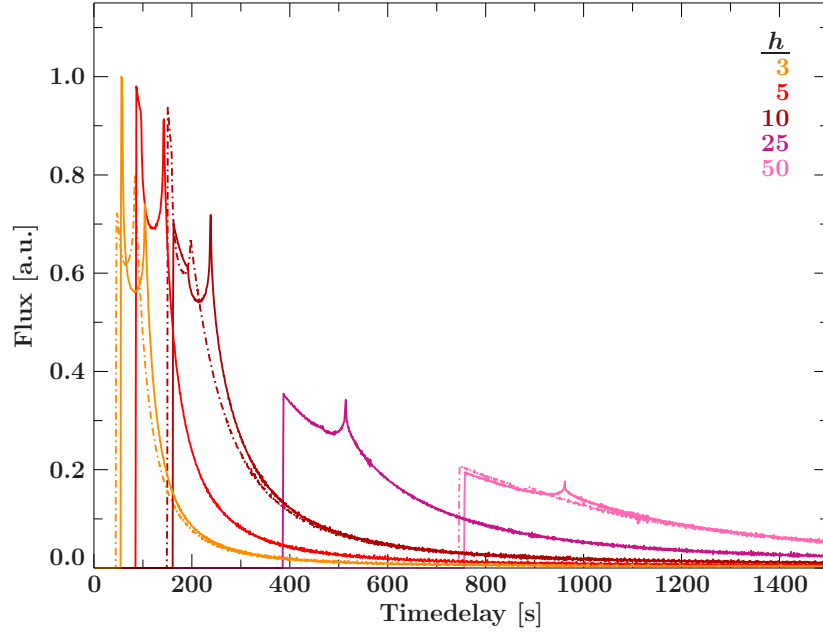


Fig. 3.23: Dependency of the time delay on the height (in  $r_s$ ) of the primary source.  $H/r_{\text{out}} = 0.3$ ,  $i = 40^\circ$ ,  $\zeta = 2.0$ ,  $r_{\text{out}} = 10^3 r_s$ . Solid lines represent general relativistic time lags, dashed-dotted lines Euclidean time lags.

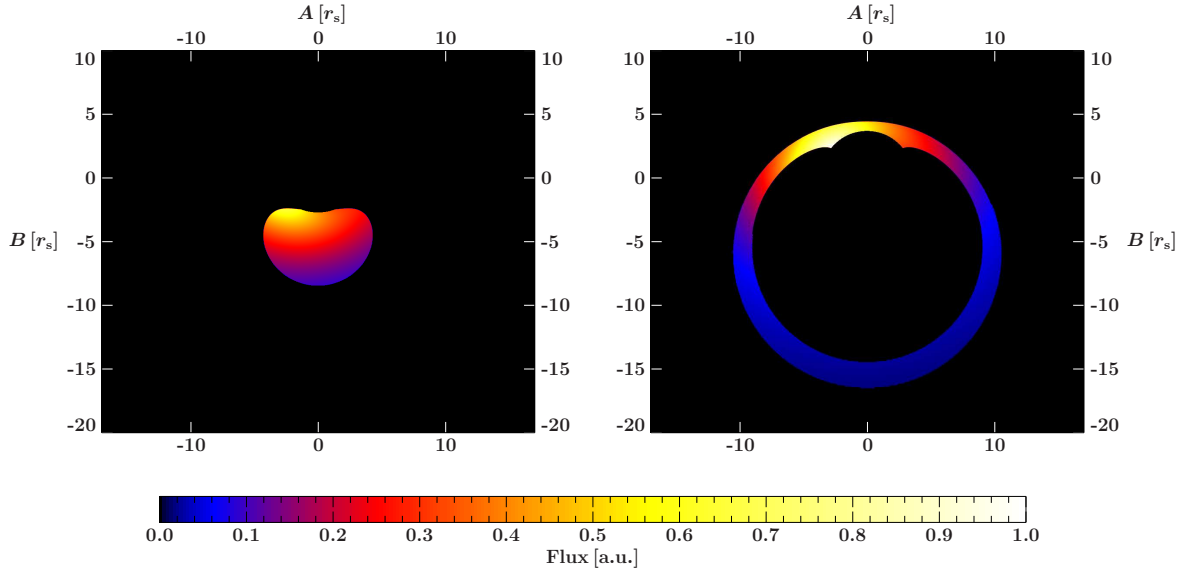


Fig. 3.24: Flux map of the regions that contribute to the peaks in the time lag for the system described by  $i = 30^\circ$ ,  $h = 5r_s$ ,  $H/r_{\text{out}} = 0.3$ ,  $\zeta = 2.0$  and  $r_{\text{out}} = 10^3 r_s$ . In the left panel the flux for time delays of 98 – 108s is shown, in the right for 135 – 145s, respectively.

there are significant contributions from major radii, which may lead to different time lags for more physical models of the disc.

In addition, this confirms the arguments for the relevant region of the time lag in Section 3.8.2.

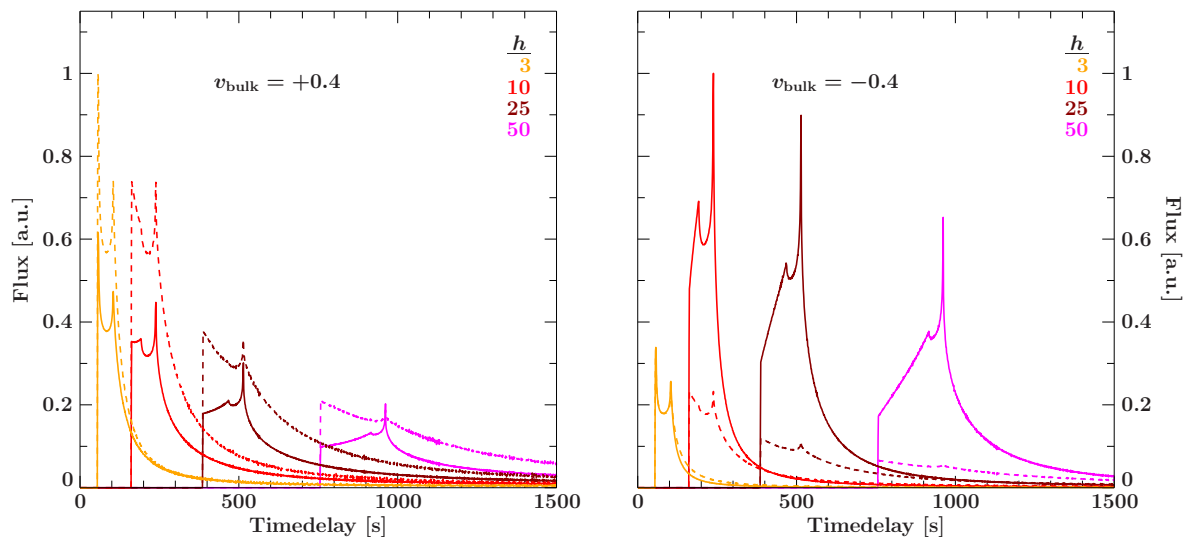


Fig. 3.25: Time lags for an anisotropic source moving towards (right panel) and away from the observer (left panel) in solid lines. For comparison the time delay of the static, spherical source is plotted in addition (dashed line). The latter is exactly the same in both cases, the two plots are normalized differently.

### 3.10 TIME LAGS FOR ANISOTROPIC SOURCES

In Section 3.1.1 the consequences of substituting the spherical source by an anisotropic source with bulk velocity  $v_{\text{bulk}}$  were discussed. The effect of such a change on the time lag is shown in Fig. 3.25. As said before, the differences in the incident flux of the accretion disc are stronger for large heights  $h$  of the primary source above the disc. This is reflected in the time lags. For  $h = 3r_s$  and  $h = 10r_s$  the time delay for the source moving towards the black hole is essentially unchanged. Note that it is actually the shape of the curve that matters, not the total flux. Differences in the first can be distinguished in an observation. This is not possible for two curves that differ just by their amplitude, as long as the total flux is not known.

For the source moving away from the black hole there is already a striking difference to the steady source for  $h = 10$ : the peak at lower time delay transforms into a plateau. An interesting fact is that besides the different total flux the shape of the curves for both directions of source motion becomes the same for even larger height  $h$ . The most characteristic feature is a very narrow peak, in contrast to the more or less flat continuum for the case of the static source. The flux for very low as well as for very high time delays decreases, since it originates from the outer region of the disc. This leads to an almost linear increase of flux at lower lags.

### 3.11 TRANSFER FUNCTIONS

So far we were looking at the spectra of the iron line and the time delays individually. But they are actually connected, since it is the same radiation carrying the one information or the other. Figure 3.26 shows a transfer function, where the energy spectrum is plotted against the time lag. It illustrates the dynamical spectrum of the iron line, i.e., flux of which energy is measured at which time. Figure 3.26 shows an example of such a transfer function for a flared accretion disc with parameters  $i = 70^\circ$ ,  $h = 5r_s$ ,  $H/r_{\text{out}} = 0.3$ ,  $\zeta = 2.0$ ,  $r_{\text{out}} = 10^3 r_s$ . What

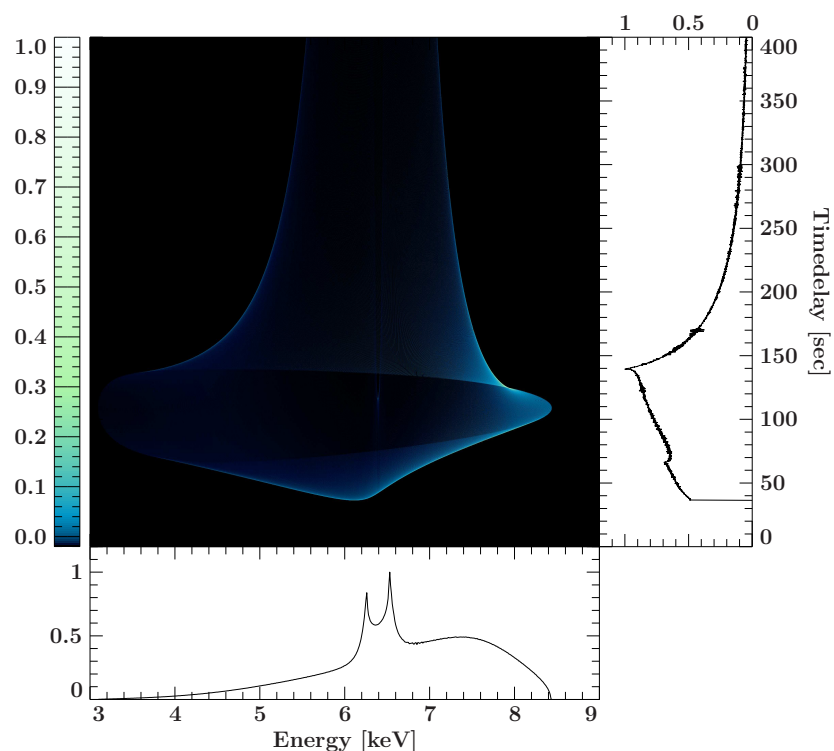


Fig. 3.26: *Transfer function for energy and time delay. As the broad iron lines consist of photons of a wide range of energies, which originate from different regions of the accretion disc, their respective time delays are different as well. This graph illustrates the frequency-dependency of the time delay of such an energy spectrum.*

we see is that most of the photons with moderate energy shifts reach the observer first, then their arrival rate decreases over a long time. Radiation with large energy shift in contrast is measured in a short time interval.

Without further discussion, some more transfer functions for different sets of parameters are presented in Fig. 3.27 to 3.36.

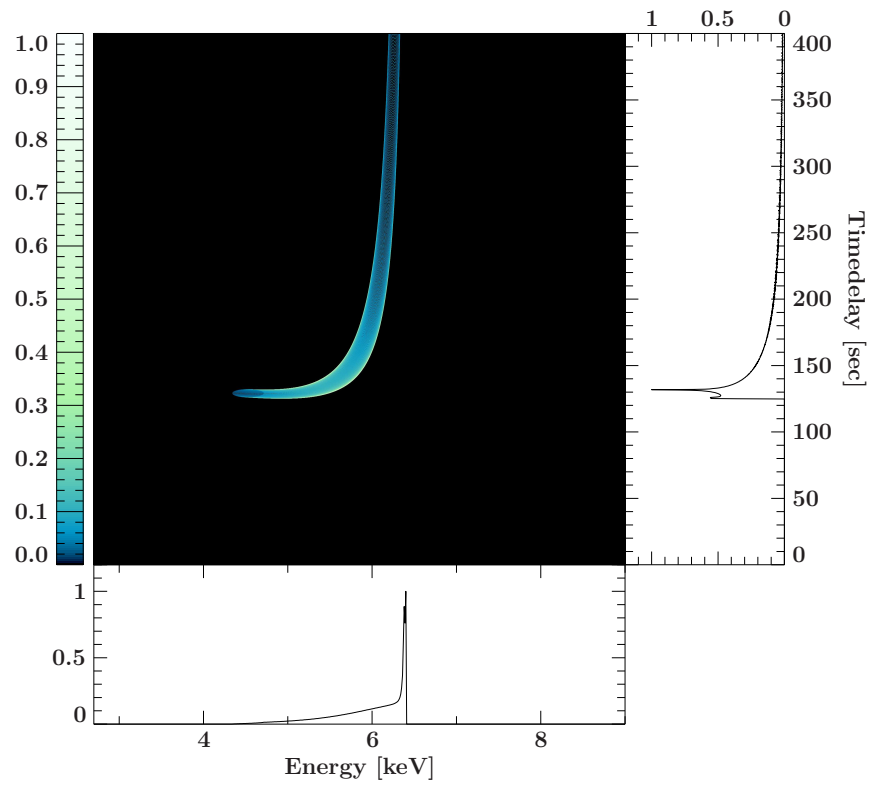


Fig. 3.27: *Dynamical spectrum:  $i = 5^\circ$ ,  $h = 5r_s$ ,  $H/r_{\text{out}} = 0.3$ ,  $\zeta = 2.0$ ,  $r_{\text{out}} = 10^3 r_s$ .*

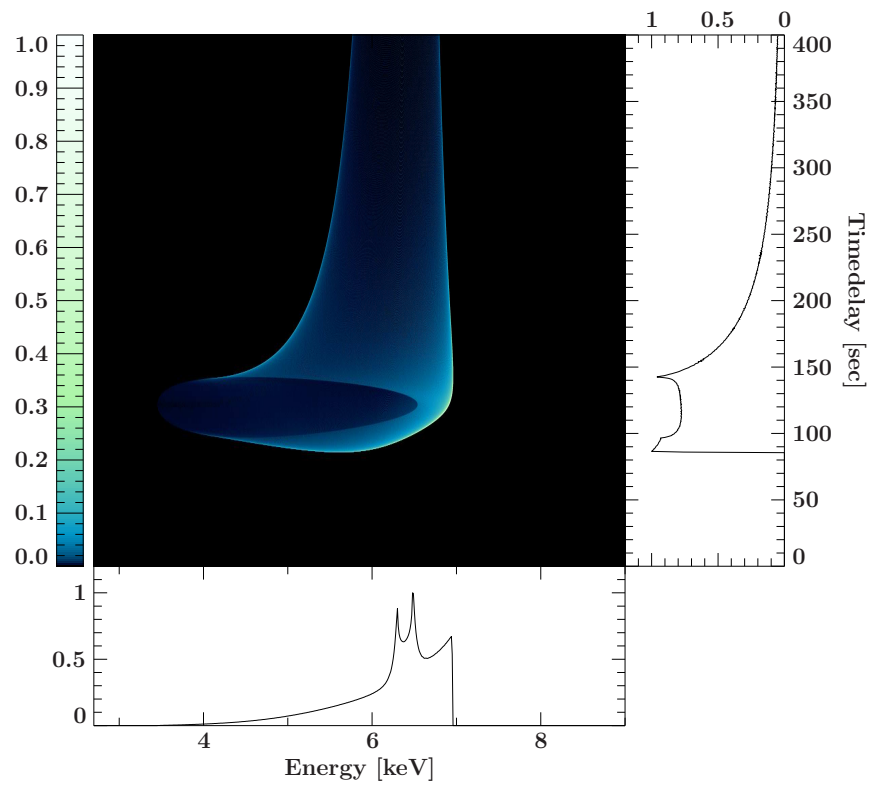


Fig. 3.28: *Dynamical spectrum:  $i = 40^\circ$ ,  $h = 5r_s$ ,  $H/r_{\text{out}} = 0.3$ ,  $\zeta = 2.0$ ,  $r_{\text{out}} = 10^3 r_s$ .*

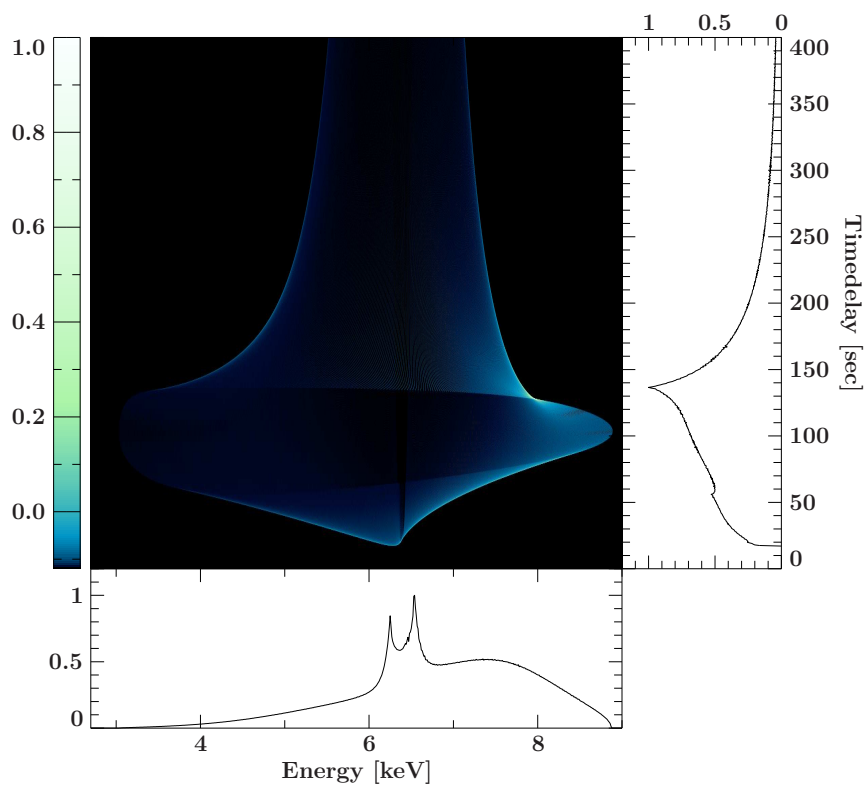


Fig. 3.29: *Dynamical spectrum:  $i = 80^\circ$ ,  $h = 5r_s$ ,  $H/r_{\text{out}} = 0.3$ ,  $\zeta = 2.0$ ,  $r_{\text{out}} = 10^3 r_s$ .*

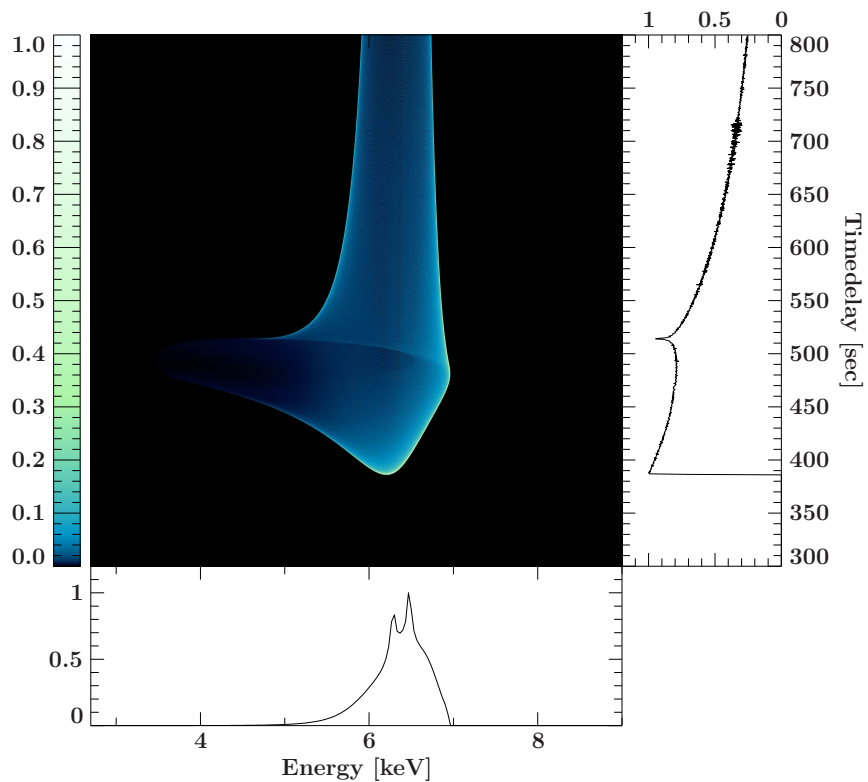


Fig. 3.30: *Dynamical spectrum:  $i = 40^\circ$ ,  $h = 25r_s$ ,  $H/r_{\text{out}} = 0.3$ ,  $\zeta = 2.0$ ,  $r_{\text{out}} = 10^3 r_s$ .*

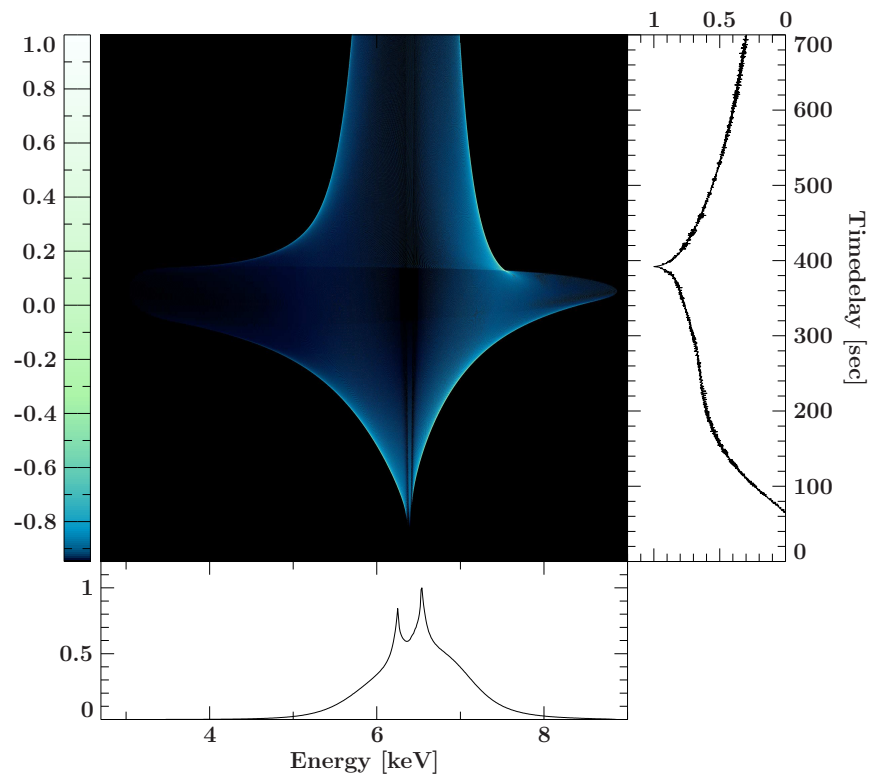


Fig. 3.31: *Dynamical spectrum:  $i = 80^\circ$ ,  $h = 25r_s$ ,  $H/r_{\text{out}} = 0.3$ ,  $\zeta = 2.0$ ,  $r_{\text{out}} = 10^3 r_s$ .*

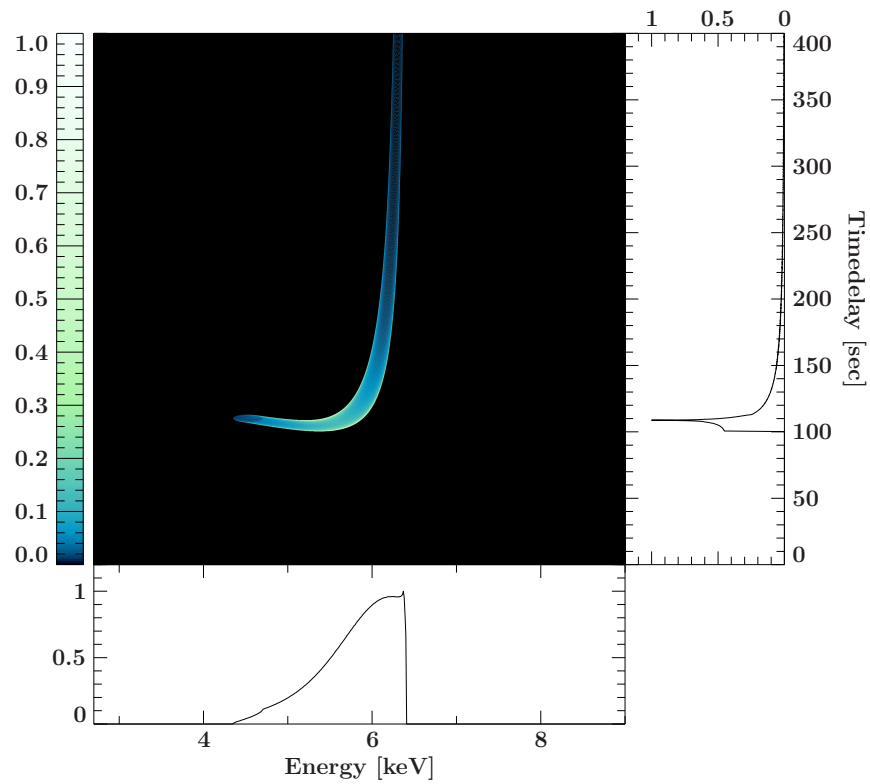


Fig. 3.32: *Dynamical spectrum:  $i = 5^\circ$ ,  $h = 5r_s$ ,  $H/r_{\text{out}} = 0.3$ ,  $\zeta = 1.0$ ,  $r_{\text{out}} = 10^3 r_s$ .*

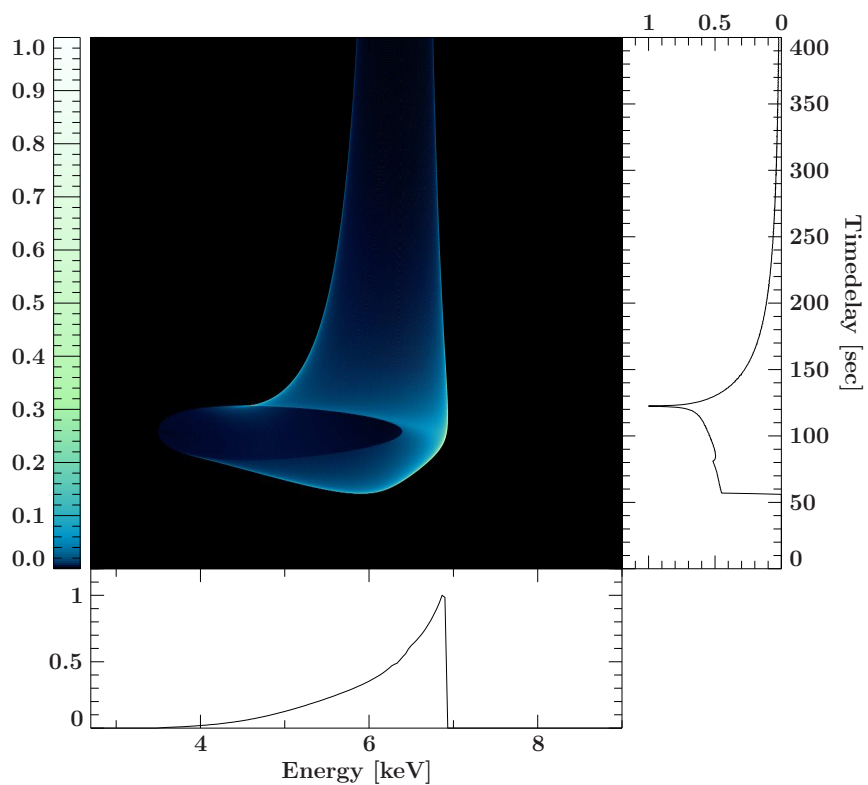


Fig. 3.33: *Dynamical spectrum:  $i = 40^\circ$ ,  $h = 5r_s$ ,  $H/r_{\text{out}} = 0.3$ ,  $\zeta = 1.0$ ,  $r_{\text{out}} = 10^3 r_s$ .*

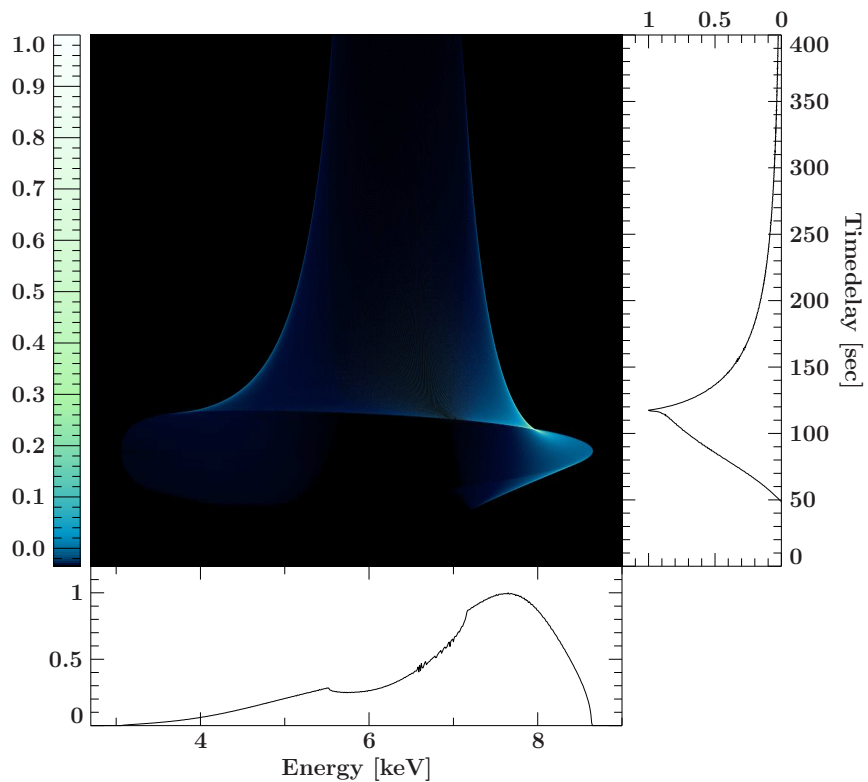


Fig. 3.34: *Dynamical spectrum:  $i = 80^\circ$ ,  $h = 5r_s$ ,  $H/r_{\text{out}} = 0.3$ ,  $\zeta = 1.0$ ,  $r_{\text{out}} = 10^3 r_s$ .*

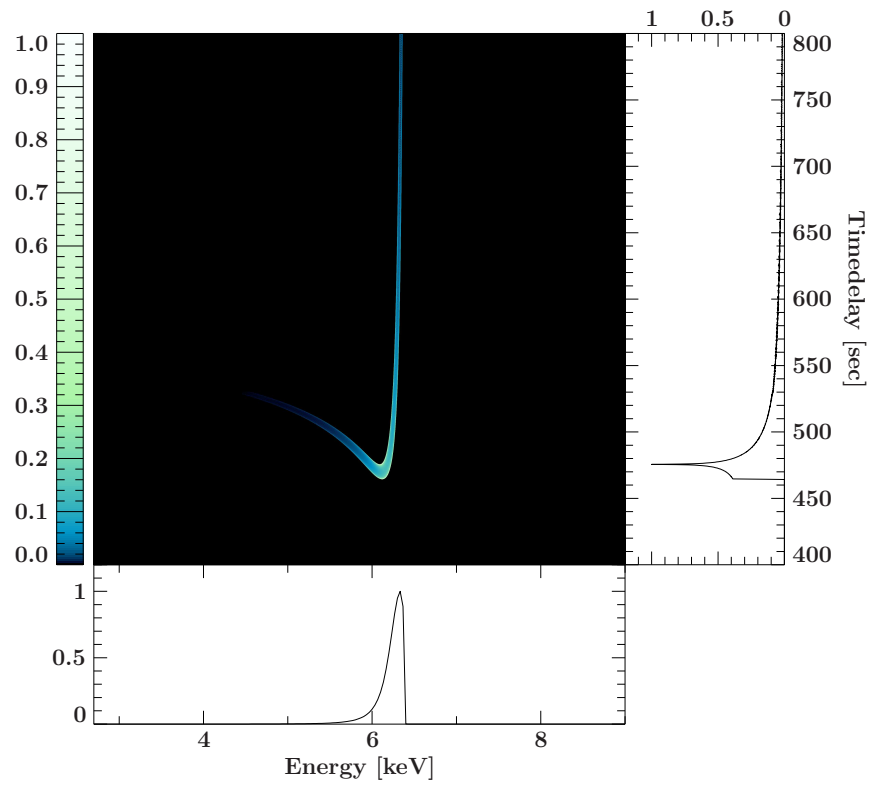


Fig. 3.35: *Dynamical spectrum:  $i = 2^\circ$ ,  $h = 25r_s$ ,  $H/r_{\text{out}} = 0.3$ ,  $\zeta = 1.0$ ,  $r_{\text{out}} = 10^3 r_s$ .*

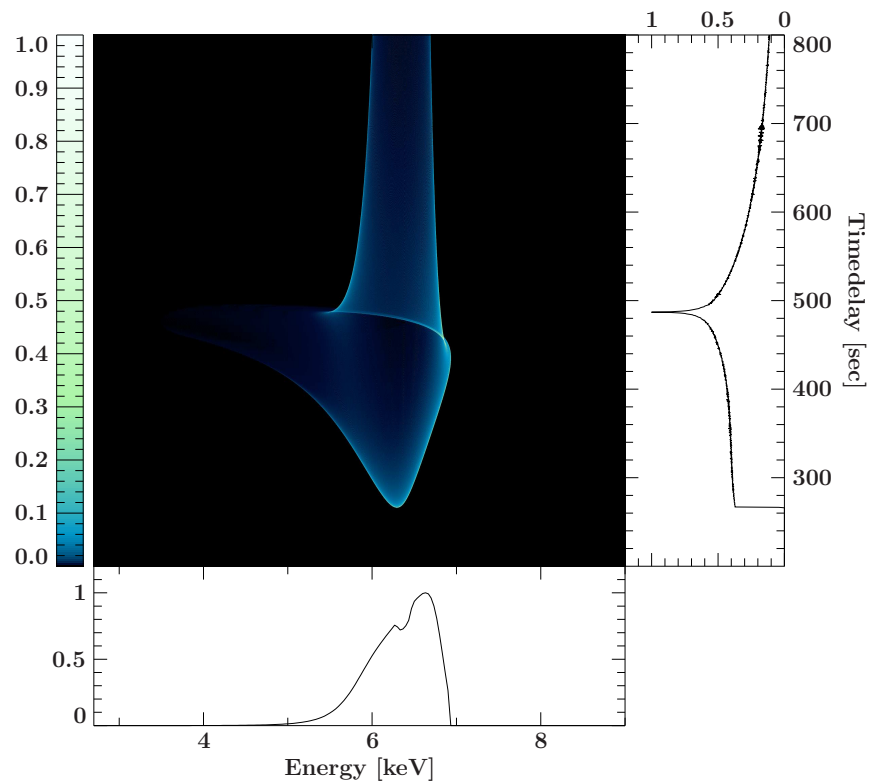


Fig. 3.36: *Dynamical spectrum:  $i = 40^\circ$ ,  $h = 25r_s$ ,  $H/r_{\text{out}} = 0.3$ ,  $\zeta = 1.0$ ,  $r_{\text{out}} = 10^3 r_s$ .*

---

## CHAPTER 4

# CONCLUSION AND OUTLOOK

---

The presented results demonstrate the necessity of the chosen general relativistic approach. Existing results could be reproduced and further insights into the principle of reverberation mapping were obtained. The presented characteristic signatures of the parameters of the system in the measured time lags give the basis to constrain them for measured data.

In order to apply it to actual observational data it is necessary to further develop the model into a more physically one. Some relevant possible extension are presented below.

Current observations suggest, that many known black holes (or black hole candidates) have high or intermediate spin. Figure 4.1 shows the mass and spin parameters of 19 supermassive black holes, based on observations of the XMM-Newton, Suzaku and NuSTAR satellites (Reynolds, 2013). Therefore, an extension of the model for rotating black holes seems necessary. This means approaching all the performed calculations in the Kerr metric, at least close to the black hole where the differences to the Schwarzschild spacetime are significant. For the illumination of the accretion disc this has already partly been done.

Aside from these changes of the underlying theory, there are other aspects that were not considered. Nayakshin (2001) showed, that the ionization state of the accretion disc alters

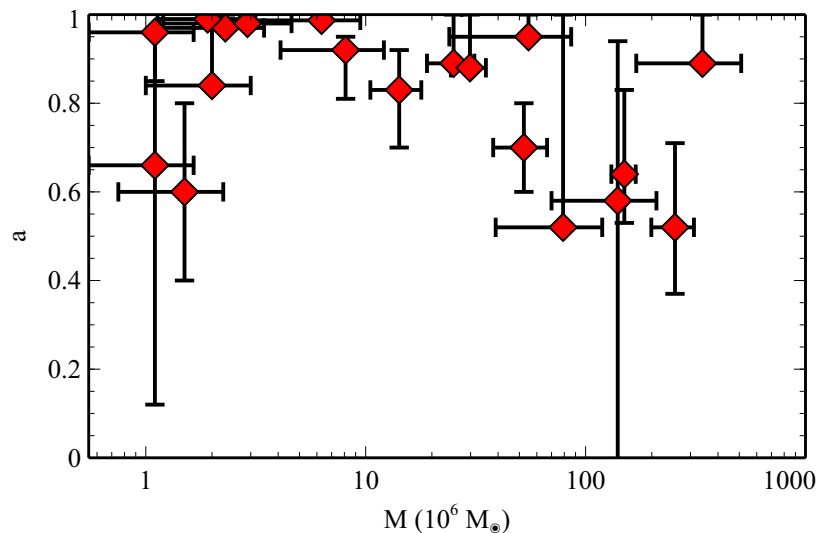


Fig. 4.1: Masses and spin parameters for 19 supermassive black holes. Picture taken from Reynolds (2013).

---

the spectral shape of observed emission lines, so ionization physics should be included in the simulation.

Another point at which a generalization is reasonable is the primary source which irradiates the disc. Although, as stated before, the current knowledge about the nature of this source is limited, one can certainly start from the premise that it is not point like, or even close to it. So considering extended sources would be another step to a more realistic model. The exact shape and characteristics of such extended sources can be manifold. Moreover, such a simulation could help to constrain their nature by applying it to data.

This leads to another, more technical point. So far all the parameters of the system are just input which lead to an certain result. For the application of the model to observed data the procedure would be the other way round. For example, a time lag is obtained by cross correlation of satellite data. The goal then is to fit all the parameters to this time lag and hopefully constrain them that way. In order to do so, a fit function and the necessary database for the parameter dependency has to be developed.

So far all the discussions ignored any impact of other objects than the black hole, the irradiating source, and the accretion disc. This is of course a simplification. The black hole system consists of more than that. The current model of AGN predicts that outside the disc there is a obscuring torus and large clouds of gas (Longair, 2011). This leads to absorption effects which have been discussed by, e.g., Bianchi et al. (2012). A combination with such absorption models would lead to a better understanding of observations.

---

# ACKNOWLEDGMENTS

---

First of all i want to thank my supervisor Jörn Wilms for giving me the opportunity to write my thesis on this exciting topic and all his helpful comments and support.

Furthermore i would like to thank all the people at the observatory. My office colleagues Felicia Krauss, Christian Schmid and Michael Wille for their helpful advice in many situations, interesting discussions and general attitude that made working here so pleasant. Sebastian Falkner for lots of fruitful discussions on many topics. The drivers from Erlangen, who made working here possible in the first place. The other Remeisen for all the nice activities and conversations, work related or not. All of them make this place an enjoyable one to work and to be at.

Special thanks deserves Thomas Dauser for his support throughout the last year, his good advice in many situations and numerous discussions.

Last but not least i want to thank my family for their support over the last years.

---

# REFERENCES

---

- Antonucci R., 1993, *ARA&A* 31, 473
- Bardeen J.M., Press W.H., Teukolsky S.A., 1972, *ApJ* 178, 347
- Beloborodov A.M., 1999, *Astrophys. J., Lett.* 510, L123
- Bianchi S., Maiolino R., Risaliti G., 2012, *Advances in Astronomy 2012*
- Blandford R.D., McKee C.F., 1982, *ApJ* 255, 419
- Carroll S.M., 2004, *Spacetime and geometry. An introduction to general relativity*, Addison Wesley
- Cassatella P., Uttley P., Wilms J., Poutanen J., 2011, In: Ness J.U., Ehle M. (eds.) *The X-ray Universe 2011.*, p. 54
- Cassatella P., Uttley P., Wilms J., Poutanen J., 2012, *MNRAS* 422, 2407
- Chandrasekhar S., 1983, *The mathematical theory of black holes*
- Dauser T., Garcia J., Wilms J., et al., 2013, *MNRAS* 430, 1694
- Dauser T., Wilms J., Reynolds C.S., Brenneman L.W., 2010, *MNRAS* 409, 1534
- Dovčiak M., Muleri F., Goosmann R.W., et al., 2012, *Journal of Physics Conference Series* 372, 012056
- Einstein A., 1916, *Annalen der Physik* 354, 769
- Falkner S., Dauser T., Falanga M., Wilms J., 2013, *Diploma thesis, University of Erlangen-Nuremberg*
- Ferrarese L., Ford H.C., Jaffe W., 1996, *apj* 470, 444
- Fließbach T., 1990, *Allgemeine Relativitätstheorie.*, BI Wissenschaftsverl.
- Frank J., King A.R., Raine D.J., 1995, *Astronomische Nachrichten* 316, 414
- Fukumura K., Kazanas D., 2007, *ApJ* 664, 14
- George I.M., Fabian A.C., 1991, *MNRAS* 249, 352
- Hawking S.W., 1974, *Nat* 248, 30
- Kerr R.P., 1963, *Physical Review Letters* 11, 237
- Krolik J.H., 1999, *Active galactic nuclei : from the central black hole to the galactic environment*
- Laor A., 1991, *ApJ* 376, 90
- Longair M.S., 2011, *High Energy Astrophysics*
- Markoff S., Falcke H., Fender R., 2001 372, L25
- Marscher A.P., 2006, In: Hughes P.A., Bregman J.N. (eds.) *Relativistic Jets: The Common Physics of AGN, Microquasars, and Gamma-Ray Bursts*, Vol. 856. American Institute of Physics Conference Series, p.1
- Misner C.W., Thorne K.S., Wheeler J.A., 1973, *Gravitation*
- Nandra K., Pounds K.A., 1994, *MNRAS* 268, 405
- Nayakshin S., 2001, *Advances in Space Research* 28, 425
- Netzer H., Peterson B.M., 1997, In: Maoz D., Sternberg A., Leibowitz E.M. (eds.) *Astronomical Time Series*, Vol. 218. *Astrophysics and Space Science Library*, p. 85
- Pechenick K.R., Ftaclas C., Cohen J.M., 1983, *ApJ* 274, 846
- Poutanen J., 2002, *MNRAS* 332, 257
- Poutanen J., Beloborodov A.M., 2006, *MNRAS* 373, 836
- Pozo Nuñez F., Ramolla M., Westhues C., et al., 2012 545, A84
- Press W.H., Teukolsky S.A., Vetterling W.T., Flannery B.P., 1992, *Numerical recipes in C. The art of scientific computing*
- Rees M.J., Begelman M.C., Blandford R.D., Phinney E.S., 1982, *Nat* 295, 17
- Reynolds C.S., 2013, *ArXiv e-prints*
- Rybicki G.B., Lightman A.P., 1980 59, 509
- Schwarzschild K., 1916, *Abh. Konigl. Preuss. Akad. Wissenschaften Jahre 1906,92*, Berlin, 1907 189–196
- Shakura N.I., Sunyaev R.A., 1973 24, 337
- Sunyaev R.A., Titarchuk L.G., 1980 86, 121
- Thorne K.S., 1974, *ApJ* 191, 507
- Wilkins D.R., Fabian A.C., 2012, *MNRAS* 424, 1284

---

# DECLARATION

---

Hiermit erkläre ich, dass ich die Arbeit selbstständig angefertigt und keine anderen als die angegebenen Hilfsmittel verwendet habe.

Bamberg, 12.09.2013

---

Fabian Brod